THE THERMAL EMISSION IMAGING SYSTEM (THEMIS) FOR THE MARS 2001 ODYSSEY MISSION

PHILIP R. CHRISTENSEN[1*], BRUCE M. JAKOSKY[2], HUGH H. KIEFFER[3], MICHAEL C. MALIN[4], HARRY Y. MCSWEEN, JR.[5], KENNETH NEALSON[6], GREG L. MEHALL[7], STEVEN H. SILVERMAN[8], STEVEN FERRY[8], MICHAEL CAPLINGER[4] and MICHAEL RAVINE[4]

[1]*Department of Geological Sciences, Arizona State University, Tempe, AZ 85287-1404, U.S.A.*
[2]*Laboratory of Atmospheric and space Physics and Department of Geological Sciences, University of Colorado, Boulder, CO 80309, U.S.A.*
[3]*U.S. Geological Survey, Flagstaff, AZ 86001, U.S.A.*
[4]*Malin Space Science Systems, San Diego, CA 92121, U.S.A.*
[5]*Department of Geological Sciences, University of Tennessee, Knoxville, TN 37996-1410, U.S.A.*
[6]*Jet Propulsion Laboratory, Pasadena, CA 91006, U.S.A.*
[7]*Department of Geological Sciences, Arizona State University, Tempe, AZ 85287-1404, U.S.A.*
[8]*Raytheon Santa Barbara Remote Sensing, Goleta, CA, U.S.A.*
*(*Author for correspondence, E-mail: phil.christensen@asu.edu)*

(Received 4 August 2001; Accepted in final form 6 December 2002)

Abstract. The Thermal Emission Imaging System (THEMIS) on 2001 Mars Odyssey will investigate the surface mineralogy and physical properties of Mars using multi-spectral thermal-infrared images in nine wavelengths centered from 6.8 to 14.9 μm, and visible/near-infrared images in five bands centered from 0.42 to 0.86 μm. THEMIS will map the entire planet in both day and night multi-spectral infrared images at 100-m per pixel resolution, 60% of the planet in one-band visible images at 18-m per pixel, and several percent of the planet in 5-band visible color. Most geologic materials, including carbonates, silicates, sulfates, phosphates, and hydroxides have strong fundamental vibrational absorption bands in the thermal-infrared spectral region that provide diagnostic information on mineral composition. The ability to identify a wide range of minerals allows key aqueous minerals, such as carbonates and hydrothermal silica, to be placed into their proper geologic context. The specific objectives of this investigation are to: (1) determine the mineralogy and petrology of localized deposits associated with hydrothermal or sub-aqueous environments, and to identify future landing sites likely to represent these environments; (2) search for thermal anomalies associated with active sub-surface hydrothermal systems; (3) study small-scale geologic processes and landing site characteristics using morphologic and thermophysical properties; and (4) investigate polar cap processes at all seasons. THEMIS follows the Mars Global Surveyor Thermal Emission Spectrometer (TES) and Mars Orbiter Camera (MOC) experiments, providing substantially higher spatial resolution IR multi-spectral images to complement TES hyperspectral (143-band) global mapping, and regional visible imaging at scales intermediate between the Viking and MOC cameras.

The THEMIS uses an uncooled microbolometer detector array for the IR focal plane. The optics consists of all-reflective, three-mirror anastigmat telescope with a 12-cm effective aperture and a speed of f/1.6. The IR and visible cameras share the optics and housing, but have independent power and data interfaces to the spacecraft. The IR focal plane has 320 cross-track pixels and 240 down-track pixels covered by 10 $\sim$1-μm-bandwidth strip filters in nine different wavelengths. The visible camera has a 1024 $\times$ 1024 pixel array with 5 filters. The instrument weighs 11.2 kg, is 29 cm by 37 cm by 55 cm in size, and consumes an orbital average power of 14 W.

Space Science Reviews **110:** 85–130, 2004.

1. Introduction

A major goal of the Mars Exploration Program is to obtain data that will help determine whether life ever existed on Mars. This goal will ultimately be addressed via detailed *in situ* studies and eventual return to the Earth of samples of the martian surface. It is therefore essential to identify future landing sites with the highest probability of containing samples indicative of early pre-biotic or biotic environments. Of particular interest are aqueous and/or hydrothermal environments in which life could have existed, or regions of current near-surface water and/or heat sources [*Exobiology Working Group*, 1995]. The search for these environments requires detailed geologic mapping of key sites and accurate interpretations of the composition and history of these sites in a global context.

The Thermal Emission Imaging System (THEMIS) will contribute to these goals through the global mapping of unique compositional units and the identification of key minerals and rock types. This mapping will be accomplished at spatial scales that permit mineral and rock distributions to be related to the geologic processes and history of Mars. The specific objectives of the THEMIS investigation are to: (1) determine the mineralogy of localized deposits associated with hydrothermal or sub-aqueous environments, and to identify future landing sites likely to represent these environments; (2) search for pre-dawn thermal anomalies associated with active sub-surface hydrothermal systems; (3) study small-scale geologic processes and landing site characteristics using morphologic and thermophysical properties; (4) investigate polar cap processes at all seasons using infrared observations at high spatial resolution; and (5) provide a direct link to the global hyperspectral mineral mapping from the Mars Global Surveyor (MGS) Thermal Emission Spectrometer (TES) investigation by utilizing a significant portion of the infrared spectral region at high (100 m per pixel) spatial resolution.

These objectives will be addressed using thermal infrared (6.3–15.3 μm) multispectral observations in nine wavelengths at 100-m per pixel spatial resolution, together with 18-m per pixel visible imagery in up to five colors. The thermal-infrared spectral region was selected for mineral mapping because virtually all geologic materials, including carbonates, hydrothermal silica, sulfates, phosphates, hydroxides, and silicates have fundamental infrared absorption bands that are diagnostic of mineral composition. THEMIS visible imaging provides regional coverage (with global coverage a goal) at spatial scales that are intermediate between those of Viking and the detailed views from the MGS Mars Orbiter Camera (MOC) (Malin and Edgett, 2001).

THEMIS builds upon a wealth of data form previous experiments, including the Mariner 6/7 Infrared Spectrometer (Pimentel *et al.*, 1974) the Mariner 9 Infrared Interferometer Spectrometer (IRIS) (Hanel *et al.*, 1972; Conrath *et al.*, 1973), the Viking Infrared Thermal Mapper (IRTM) (Kieffer *et al.*, 1977), the Phobos Termoscan (Selivanov *et al.*, 1989), the MGS TES (Christensen *et al.*, 2001a; Smith *et al.*, 2001c; Bandfield *et al.*, 2000a; Christensen *et al.*, 2000b, 2001b), and the MGS

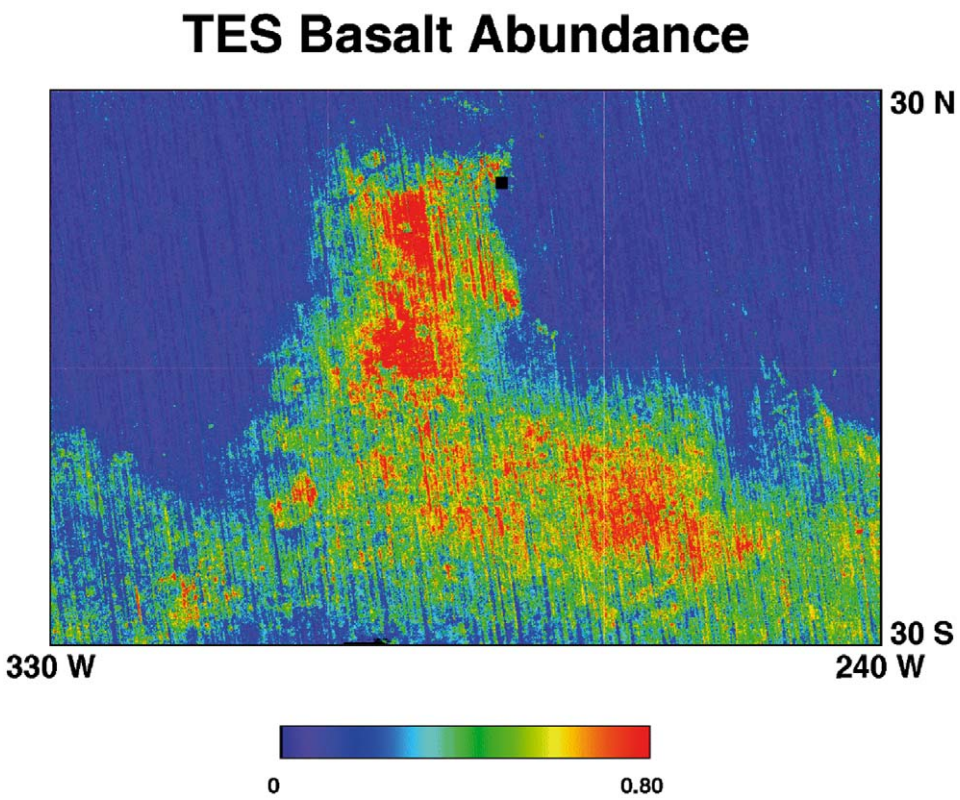

Figure 1. TES mineral map of the Syrtis Major region of Mars. The fraction of the surface covered by basalt is shown as derived from deconvolution of TES spectra. Data are from Bandfield *et al.* (2000). (a) Regional view. Black region is area shown in Figure 1b. (b) 60 km × 60 km region at TES resolution.

MOC (Malin and Edgett, 2001). In particular, the TES instrument has collected hyperspectral images (143 and 286 spectral bands) of the entire martian surface at wavelengths from 6 to 50 micrometers, providing an initial global reconnaissance of mineralogy and thermophysical properties (Christensen *et al.*, 2000b, d, 2001a; Bandfield *et al.*, 2000a; Bandfield, 2002; Ruff and Christensen, 2002; Jakosky *et al.*, 2000; Mellon *et al.*, 2000). By covering the key 6.3 to 15.0 μm region in both instruments it is possible to combine the high spectral resolution of TES with the high spatial resolution of THEMIS to achieve the goals of a global mineralogic inventory at the spatial scales necessary for detailed geologic studies within the Odyssey data resources.

Figure 1 shows a basalt abundance map derived from TES data of a region of Mars centered on Syrtis Major, illustrating the global-scale reconnaissance obtained from TES. Figure 1b shows a 60 km × 60 km region within Syrtis Major. Figure 2a shows an orbital infrared image of a 60 by 60 km area on Earth, degraded to 3 km per pixel. Figure 2b shows the same scene at 100-m per pixel THEMIS

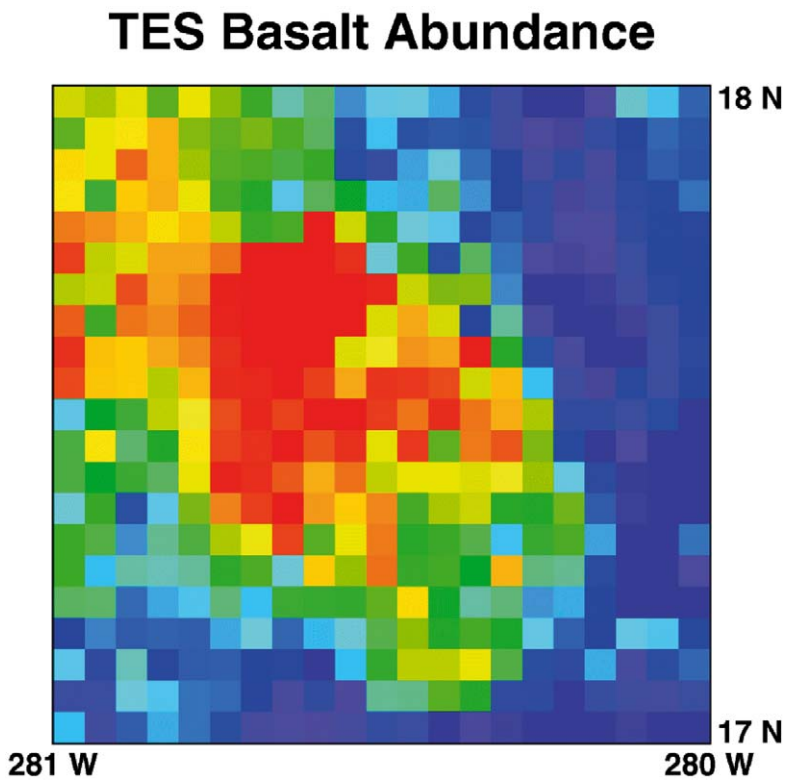

Figure 1. Continued.

resolution. Comparison of scenes at TES and THEMIS resolutions illustrates the dramatic improvement in geologic unit discrimination that is possible at THEMIS spatial resolution, and the difficulties encountered in attempting detailed studies for geologic interpretation and landing site selection using TES data alone. At THEMIS scale, terrestrial lake beds, hydrothermally altered zones, carbonate outcrops, silica-rich rocks, channel floors, and other indications of ancient aqueous environments can be readily identified and mapped using multi-spectral IR images. THEMIS can provide similar detection of such systems on Mars, if they are present at similar scales and exposed at the surface.

THEMIS data will be used to identify and map sites for future rovers and sample- return missions, beginning with the Mars 2003 Rovers, by aiding in the evaluation of the science rationale, hazards (e.g. rocks and dust), and morphology of these sites. These data will also provide information to adjust the exact location of the landing ellipses to maximize the science return, plan the '03 Rover traverses, and aid in the extrapolation of the Rover results. The Rover payloads contain miniature versions of the MGS TES instrument (Silverman *et al.*, 1999) covering the THEMIS spectral region. If both the Miniature-TES and THEMIS (and possibly TES) instruments are operating simultaneously, there will be a powerful link from

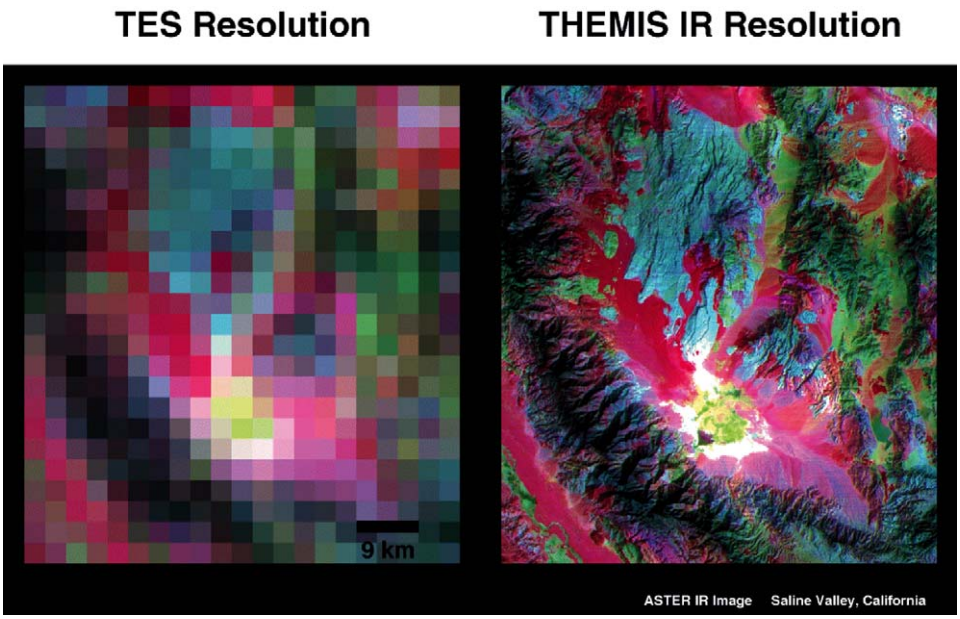

Figure 2. Comparison of TES and THEMIS spatial resolution. Both image sets are IR 3-band visible images of the Saline Valley, California acquired by the ASTER instrument on the Terra spacecraft. ASTER image. (a) Simulated 3-km per pixel TES resolution. (b) THEMIS 100-m per pixel resolution. Individual channels, lake beds, silica-rich outcrops and sediments, and lava flows can be spatially distinguished and compositionally identified. These data have been made available by NASA, GSFC, MITI, ERSDAC, JAROS, and the U.S./Japan ASTER Science Team.

the meter scale viewed by mini-TES to the 100-m scale of THEMIS to the global mapping of MGS TES.

2. Mars Science Questions

A primary objective of the Mars Exploration Program is to understand the biotic and pre-biotic environments of Mars. Key questions can be divided into two broad categories: (1) the search for aqueous environments, both ancient and active, that provide insight into biotic and pre-biotic conditions; and (2) the understanding changes in environmental conditions, climate, and geologic processes through time.

2.1. AQUEOUS ENVIRONMENTS

A major scientific focus of the Mars Program is the exploration of Mars as a possible abode for life. This exploration will be done by the global reconnaissance of Mars to understand the geological and volatile history, the detailed investigation of

sites of exobiological interest, and the in-depth *in situ* exploration of some of these sites using rovers, culminating in the return of samples from one or more sites.

Although there is much that we do not know about the origin of life, the necessary environmental conditions appear to consist of: (i) the presence of liquid water, as a medium of transport for nutrients and waste products; (ii) the presence of the biogenic elements, consisting of C, H, O, N, S, P, Ca, Fe, and other trace elements that participate in life; and (iii) a source of energy that can drive chemical disequilibrium, so that the 'slide' back towards equilibrium can drive biochemical reactions (e.g., Jakosky, 1998). Mars appears to have (or have had) all of these ingredients:

(i) Evidence for liquid water is widespread on Mars (e.g. Carr, 1996). The ancient, heavily cratered surfaces (older than about 3.5 b.y.) are dissected by valley networks; the role of liquid water in their formation is clear, even though the exact mechanism of formation is being debated (Malin and Carr, 1999). In addition, there has been dramatic sedimentation and erosion on these surfaces, evidenced by the presence of extensive layered deposits (Malin and Edgett, 2000), the distribution of small impact craters, and the severe degradation of larger craters (e.g. Craddock and Maxwell, 1993; Craddock *et al.*, 1997). The high deposition and erosion rates, the catastrophic outflow channels, and the presence of morphological features such as layers and gullies in partly eroded craters, can best be explained by liquid water (e.g. Carr, 1996). Apparently, water was more stable and abundant near the surface of early Mars than it is today.

(ii) Mars appears to have all of the biogenic elements readily accessible at the surface or in the crust. This is not surprising given the active geological environment that has existed for 4 b.y. In particular, carbon is present in the atmosphere in a readily usable form (CO_2) that also can dissolve in water and percolate into the crust. In addition, *in situ* measurements from the Viking and Pathfinder landers, together with studies of the martian meteorites, indicate the presence of all of the other elements necessary to support life (e.g. McSween, 1994; Bell *et al.*, 2000).

(iii) Volcanism has occurred on Mars throughout time, and can provide a ready source of easily accessed geothermal energy. On Earth, volcanic heat is tapped by the circulation of water through hydrothermal systems. As the water is released back to the surface, chemical potential drives the formation of organic molecules that can serve as a reducing agent to do useful work (Shock, 1997). Such hydrothermal systems may have served as the location for the terrestrial origin of life, and may have been widespread on Mars given the abundant volcanism and crustal water (Jakosky and Shock, 1998).

Among the most likely sites to search for life are regions where liquid water was present for substantial periods of time. A great deal of work has been done to define the characteristics of such sites and to identify the environments that are conducive both to the sustenance of life and to the preservation of evidence of this life (McKay *et al.*, 1996; Boston *et al.*, 1992; Walter and Des Marais, 1993). Lacustrine sediments have been identified as logical targets both as evidence of an

aqueous environment and because fossils are often preserved there. A second high priority target would be ancient thermal springs, where life could have existed and be well preserved in unique, remotely identifiable mineral deposits (Walter and Des Marais, 1993).

The characteristics of terrestrial spring deposits provide a context in which to search for similar martian deposits. These deposits derive from the intense hydrothermal weathering of the country rock. Silica, in the form of amorphous silica, quartz, chalcedony, and opaline silica, is the most common precipitate formed in volcanic terrains (Ellis and McMahon, 1977), due to both the high solubility of silica in hot water and the rapid decrease in solubility with decreasing temperature. Silica is also an excellent preservation media and is an ideal candidate site in the search for ancient life on Mars (Walter and Des Marais, 1993). Silica-depositing springs are abundant in a wide range of volcanic compositions on Earth, occurring in both rhyolitic (e.g., Yellowstone) and basaltic (e.g., Iceland) regions (Brock, 1978). The Yellowstone region is an excellent example of a THEMIS target. It contains $\sim$ 3,000 springs spread over an 80 by 100 km area, with zones of intense hydrothermal alteration up to several km in size (White *et al.*, 1988).

Calcium carbonate deposits (travertine) are also common in hydrothermal systems. Hydrothermal travertine forms by degassing of hot ($\sim$60–100 °C) Ca- and CO_2-rich groundwater, followed by precipitation of calcium carbonate (Ellis and McMahon, 1977; Pentecost, 1996). Studies of travertine have indicated the common presence of organic material, including microfossils (Pentecost, 1996; Bargar, 1978).

An additional location to search for evidence of life would be deep beneath the surface, where martian biota might survive (and perhaps even thrive) in much the same way that some deep-subsurface bacteria thrive on the Earth–by metabolizing hydrogen produced by interactions between water and basalt in the pore spaces of the rock (Stevens and McKinley, 1995). Such locales on Mars might be observable in the walls of Valles Marineris, for example, where there is up to 10 km of vertical exposure of rock that were previously buried.

2.2. SURFACE MORPHOLOGY AND THE EVOLUTION OF CLIMATE

2.2.1. *Aqueous Environments and Morphology*

Aqueous environments can be distinguished by a variety of unique morphologic features. These include flow indicators, such as streamlined depositional or erosion features, layered sediments, strand lines, and delta deposits. These features can be detected with 18 m resolution, as demonstrated by the correlation between predictions for the Pathfinder site based on 38 m Viking Orbiter imagery (Golombek *et al.*, 1997) and the actual Pathfinder surface observations. Paleohydrology will be studied using images of the sequence of sediments deposited by various stages of fluvial processes. These will include variations in flow hydraulics, sediment transport characteristics, and the properties and distribution of deposits (Komatsu

and Baker, 1997). The visible images also provide excellent context images for the 100-m multi-spectral IR and nighttime temperature images, allowing the distribution of compositionally unique outcrops, deposits, or disseminated materials to be interpreted in relationship to the landscape processes.

2.2.2. *Aeolian Sediments and Morphology*

Sedimentary deposits on Mars range from micron thick dust coatings to km-thick units of layered sediments from the equator (e.g. Tanaka and Leonard, 1995; Tanaka, 1997; Malin and Edgett, 2000) to the poles (Herkenhoff and Murray, 1990b; Thomas *et al.*, 1992). Transport has been important in moving material for much of Mars' history and the transport has been global in scale. Deciphering the materials and stratigraphy of the wide variety of sedimentary deposits on Mars is crucial to understanding the geological influences of climate on Mars and the relationship of current processes to past ones.

Transport of sediments in the current climate is presently dominated by Hadley circulation in southern summer (Thomas and Gierasch, 1995; Greeley *et al.*, 1992). Many dune deposits, wind streaks, and other deposits of likely aeolian (or possibly lacustrine) origin occur. A primary goal of any study of such deposits is the search for compositional or morphologic clues to their origin, transport, and deposition. A major question exists as to the origin and depositional environments of older sedimentary rocks. Multi-spectral IR, nighttime temperature, and visible observations will be used to map the morphologies, compositional units, and physical properties in key areas identified from earlier missions.

The polar deposits, thought to be climatically sensitive because of their association with frost deposition, include at least two non-volatile components as indicated by Viking Orbiter color data (Herkenhoff and Murray, 1990a; Thomas and Weitz, 1989). The layered deposits appear to reflect cycles of deposition and erosion on a variety of time scales, and their overall extent has been reduced from previously larger deposits (Thomas *et al.*, 1992). Coverage of selected areas of the layered deposits, chasmata, deposits marginal to the layered deposits, and polar dunes with up to 14 visible and IR filters will provide discrimination of surface units beyond what is possible using Viking images, TES 5-km resolution spectra, and MOC panchromatic images. The additional compositional and particle texture discrimination available in the infrared and color image will improve the ability to discriminate and interpret spectrally distinct surface units. A spatial resolution of 18 meters per pixel permits local morphology to be associated with compositional units. This is particularly useful in relating materials exposed on dunes and wind streaks to current wind regimes, and relating morphologies to source areas, and in examining small-scale features thought to be related to seasonal frost cycling (Thomas *et al.*, 2000).

2.2.3. *Craters as Stratigraphic Probes*

In addition to layered materials revealed by erosion in crater interior deposits, canyon walls, along faults, and in the polar deposits, additional stratigraphic information can be gleaned from morphological and compositional studies of impact craters. The interior walls of such craters often reveal the layering of the materials that were impacted, while the ejecta blankets show radial compositional gradations reflecting the inversion of stratigraphy in the ejecta (e.g. Shoemaker, 1963). The visible and IR observations can be combined with spatial studies (i.e., observations of nearby craters of similar size) to trace subsurface composition and structure.

2.3. TEMPERATURE ANOMALIES

The Mars Odyssey orbit is ideally suited for the detection of pre-dawn temperature anomalies not associated with solar heating. Multi-spectral temperature maps with a noise-equivalent delta temperature (NEΔT) of 1 K will be produced for the entire planet. These data will allow identification of sites of active hydrothermal systems and potential near-surface igneous activity using the spatial distribution of temperature differences (e.g., along linear zones) to distinguish them from physical properties such as rock abundance. The discovery of active systems would radically alter our current models of the near- surface environment, and we will undertake an exploration for temperature anomalies using pre-dawn temperature measurements.

Regions to be mapped for thermal anomalies will initially focus on young volcanic sites, where mobilization of ground ice would result from intrusive or extrusive volcanic activity. Although it may be unlikely that thermal anomalies are present, their detection would so heavily influence future sampling strategies that a search for them is of high priority.

2.4. POLAR PROCESSES

The two volatiles that are key to understanding Mars climate and evolution are CO_2, as the major agent for transport and storage of energy, and H_2O, as an important geomorphic agent. Models of their physical properties, their sublimation, and their seasonal behavior have been developed which agree with the general features of existing observations, and allow some extrapolation into the past (e.g. Davies *et al.*, 1977; Kieffer, 1979, 1990; James and North, 1982; Haberle and Jakosky, 1990; Kieffer and Zent, 1992; Kieffer *et al.*, 2000). At present, however, our understanding of the martian poles is sufficiently incomplete to prevent detailed modeling and predictions of volatile behavior in either time or space. Several geophysical processes remain to be fully understood, such as the origin and seasonal behavior of unusual 'Cryptic' regions (Kieffer *et al.*, 2000), the complex physical nature of the polar ices (Kieffer *et al.*, 2000; Titus *et al.*, 2001), the incorporation of dust and water ice into the seasonal polar caps, the influence of suspended aerosols on the radiation balance over the winter cap (e.g. Paige and Ingersoll, 1985) and the processes which cause the major polar outliers.

The THEMIS investigation will address a variety of polar cap processes using moderate spectral and spatial resolution observations. Specific questions include: (1) what is the spatial and seasonal variation of polar condensates? (2) what produces the observed differences in the physical state of the surface condensates (e.g. the south polar Cryptic region (Kieffer *et al.*, 2000)); (3) what is the energy balance in the cap-atmosphere system? (4) what is the role of dust in influencing the surface frost accumulation and sublimation? and (5) what is the abundance and variability of atmospheric dust over the polar caps?

2.5. Atmospheric temperature and opacity

A range of atmospheric properties will be addressed by the THEMIS experiment, including: (1) the abundance and distribution of atmospheric dust, (2) the distribution and condensate abundance of H_2O clouds; and (3) the atmospheric temperature, which will be used to study atmospheric dynamics. THEMIS extends the systematic monitoring of temperature, dust, and water-ice clouds in the martian atmosphere begun by the Mariner 9 IRIS (Conrath *et al.*, 1973), Viking IRTM (Kieffer *et al.*, 1977; Martin, 1986), and TES investigations (Conrath *et al.*, 2000; Smith *et al.*, 2001a, 2002; Pearl *et al.*, 2001). The THEMIS instrument is greatly limited in its ability to map the vertical distribution of temperature and to observe water vapor relative to the TES. THEMIS does, however, provide observations similar to IRTM for the mapping of temperature (Kieffer *et al.*, 1977), ice (Christensen and Zurek, 1984; Tamppari *et al.*, 2000), and dust (Martin, 1986) and will extend the detailed year-to-year climate record begun by the MGS TES.

3. Thermal Infrared Remote Sensing

3.1. Thermal infrared emission spectroscopy

3.1.1. *Overview*

Surface composition can be determined remotely by two basic types of optical spectroscopy: (1) moderate-energy electronic spectroscopy, which samples the electron cloud surrounding the nucleus; and (2) low-energy vibrational spectroscopy, which samples bound atoms within a crystal structure.

Electronic transitions occur when a bound electron absorbs an incoming photon and transitions to a higher energy state. These energy states are quantized and vary with atomic composition and crystal structure, thus providing diagnostic information about the elemental and crystal structure. The transition metals, of which iron is common, have electronic transitions that occur in the visible and infrared (e.g. Burns, 1993), and visible and near-IR observations provide an excellent means for studying Fe-bearing minerals (McCord *et al.*, 1982; Singer, 1982; Morris *et al.*, 1990; Clark *et al.*, 1990; Bell *et al.*, 1990; Mustard *et al.*, 1993; Mustard and Sunshine, 1995).

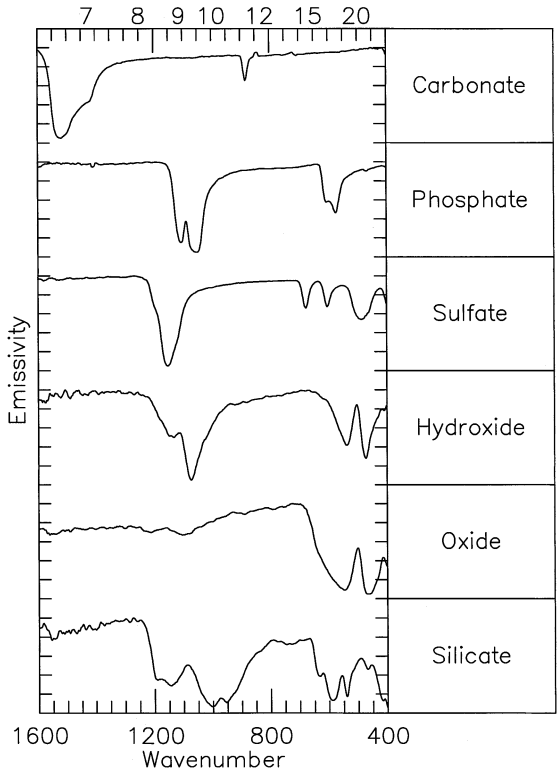

Figure 3. Thermal emission spectra of major mineral classes. These representative spectra show the significant differences in the fundamental vibrational bands between different mineral groups. Individual spectra have been offset and scaled for clarity. The band depths in these coarse particulate mineral samples have a band depth (emissivity minima) relative to the nearby local emissivity maxima of 0.2 to 0.6.

Vibrational spectroscopy is based on the principle that vibrational motions occur within a crystal lattice at frequencies that are directly related to the crystal structure and elemental composition (i.e. mineralogy) (e.g. Wilson *et al.*, 1955; Farmer, 1974). The fundamental frequencies of geologic materials typically correspond to wavelengths greater than ~ 5 μm, and provide a diagnostic tool for identifying virtually all minerals.

An extensive suite of studies over the past 35 years has demonstrated the utility of vibrational spectroscopy for the quantitative determination of mineralogy and petrology (e.g. Lyon, 1962; Lazerev, 1972; Vincent and Thompson, 1972; Farmer, 1974; Hunt and Salisbury, 1976; Salisbury *et al.*, 1987a, b, 1991; Salisbury and Walter, 1989; Bartholomew *et al.*, 1989; Salisbury, 1993; Christensen and Harrison, 1993; Lane and Christensen, 1997; Feely and Christensen, 1999; Christensen *et al.*, 2000a; Hamilton, 2000; Hamilton and Christensen, 2000; Wyatt *et al.*, 2001; Hamilton *et al.*, 2001). The fundamental vibrations within different anion groups, such as CO_3, SO_4, PO_4, and SiO_4, produce unique, well separated spectral bands

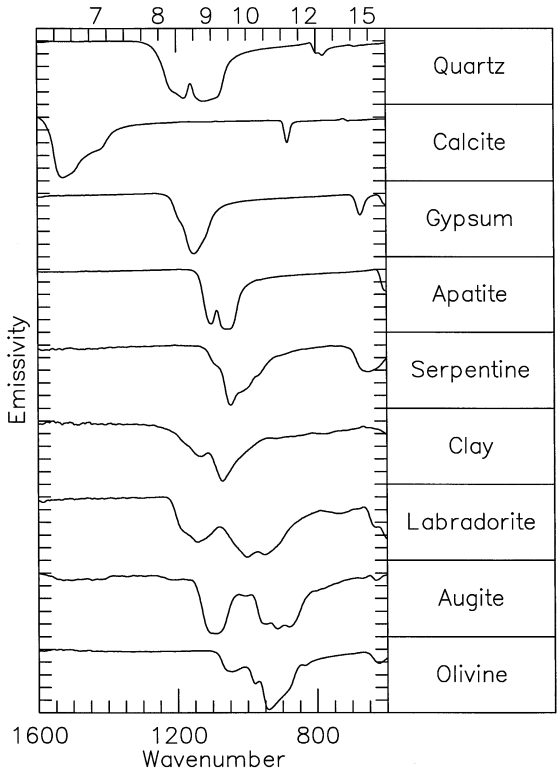

Figure 4. Thermal emission spectra of key minerals. Representative hydrothermal and aqueous minerals are shown, along with examples of the major volcanic-rock forming minerals. Individual spectra have been offset and scaled for clarity.

that allow carbonates, sulfates, phosphates, silicates, and hydroxides to be readily identified (Figure 3). Additional stretching and bending modes involving major cations, such as Mg, Fe, Ca, and Na, allow further mineral identification, such as the excellent discriminability of minerals within the silicate and carbonate groups (Figure 4). Significant progress also has been made in the development of quantitative models to predict and interpret the vibrational spectra produced by emission of energy from complex, natural surfaces (e.g. Conel, 1969; Henderson *et al.*, 1992; Hapke, 1993; Salisbury *et al.*, 1994; Moersch and Christensen, 1995; Wald and Salisbury, 1995; Mustard and Hays, 1997).

The fundamental vibrations of geologic materials typically occur between ~ 6 and 100 μm. In addition to these modes, overtone and combination vibrations, such as the 2.35 μm ($3\nu_3$) and 2.55 μm ($\nu_1 + 2\nu_3$) combination tones in carbonates (Gaffey, 1984) and the 4.5 μm ($2\nu_3$) overtone in sulfate (Blaney and McCord, 1995), also occur. These vibrations typically occur between ~ 2 and ~ 6 μm (Roush *et al.*, 1993). While they also contain important diagnostic information, these modes are typically much less populated than the fundamental vibrations (Wilson *et al.*,

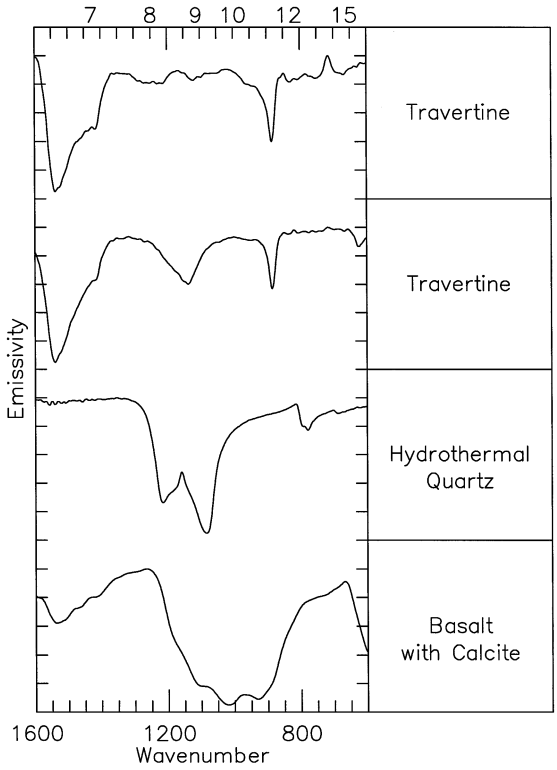

Figure 5. Thermal emission spectra of hydrothermal rocks. The travertine and hydrothermal quartz samples are from a hot-spring system within a volcanic environment. The hydrothermally altered basalt sample contains small (< 1 mm) calcite-bearing vesicles, demonstrating that < 5% carbonate can be detected in volcanic rocks. Individual spectra have been offset and scaled for clarity.

1955). As a result, the overtone and combination band absorptions in the 2–6 μm region tend to be relatively weak comparedto the fundamental absorptions in the 6 –100 μm region.

3.1.2. *Mineral Groups*

3.1.2.1. *Hydrothermal Minerals.* Thermal springs will be excellent candidates for exploration (Walter and Des Marais, 1993) and produce characteristic mineralization that is dominated by microcrystalline quartz (chert, chalcedony, opal, etc.) and carbonates. The silica minerals have a major 8–10 μm absorption (e.g. Hunt and Salisbury, 1970). Carbonates precipitate in thermal spring environments, and are the key constituents of the martian meteorite samples examined by McKay *et al.* (1996). The fundamental C-O absorption occurs near 6.7 μm (e.g. Farmer, 1974; Nash and Salisbury, 1991; Lane and Christensen, 1997) in a region that is distinct from other mineral classes (Figures 3 and 4), thereby greatly facilitating carbonate identification.

Figure 5 shows laboratory thermal emission spectra of travertine and hydrothermal silica samples collected from the Castle Hot Springs Volcanic Field of central Arizona. The distinctive spectral character of both types of hydrothermal deposits in the thermal infrared are apparent. Travertine samples are characterized by the broad absorption features typical of carbonates (calcite). The hydrothermal silica spectrum clearly exhibits the major absorption features typical of quartz. The basalt sample is an excellent analog for hydrothermal alteration on Mars. It contains small (< 1 mm) calcite-bearing vesicles and veins, similar to those found in the SNC sample ALH84001 (McKay *et al.*, 1996). The spectrum of this rock demonstrates that a small amount of carbonate ($< 5\%$) can be detected in volcanic rocks using thermal-IR spectra.

3.1.2.2. *Evaporite Minerals.* This broad class of minerals includes the following important groups: carbonates, sulfates, chlorides, and phosphates that are precipitated by the evaporation of marine or nonmarine waters. As such, they are the most obvious and direct mineralogical evidence for standing water. In the search for candidate sites for sample return, locating evaporite minerals is a high priority. The abundance of any one of these minerals in an evaporite basin is a function of the dissolved chemical constituents contained in the water as well as the history of the basin inundation/denudation. Therefore, the identification and quantification of the different evaporite minerals can yield information about the environment in which they were produced. Thermal-infrared spectra provide distinguishing characteristics for the different groups. Sulfates (gypsum) and phosphates (apatite) have deep, well-defined features in the 8.3 to 10 μm region that vary with position based on composition (Figure 4).

3.1.2.3. *Hydrous Silicates.* Minerals that incorporate hydroxyl (OH)- anions into their structure give clues about the availability of water during their formation. The majority of such minerals occur in the silicate class and most of these are in the phyllosilicate group. Within the phyllosilicates, the clay, mica, serpentine, and chlorite groups are all important. Serpentine minerals form through the activity of H_2O and ultramafic igneous rocks, so they may provide additional evidence of hydrothermal activity on Mars. Though all the hydrous silicates have the hydroxyl anion as their common trait, they range widely in their mode of occurrence. Some form as primary constituents of igneous rocks, giving clues about the magmatic conditions under which the rock was formed. Most hydrous silicates crystallize as secondary products of metamorphism and hydrothermal alteration and their composition provides insight into the pressure and temperature where they formed. Thus, the hydrous silicates serve as excellent pathfinder minerals for hydrous activity. All have characteristic mid-IR features (e.g. Figure 4) due to fundamental bending modes of $(OH)^-$ attached to various metal ions, such as an AL-O-H bending mode near 11 μm in kaolinite clay (e.g. Farmer, 1974; Van der Marel and Beeutelspacher, 1976).

3.1.2.4. *Igneous Silicates.* The primary silicate minerals associated with igneous rocks are the most abundant mineral class found on Mars (Christensen *et al.*, 2000b, 2001a; Bandfield *et al.*, 2000a; Bandfield, 2002). The majority of martian rocks likely will vary by only relatively subtle differences in bulk mineralogy, represented by the common rock forming minerals. An ability to distinguish and quantify olivines, pyroxenes, and feldspars is crucial to describing the geological character of the planet. Without this overview, the locations of hydrous activity are without context. All silicates have Si-O stretching modes between 8 and 12 μm that vary in position with mineral structure (e.g. Figure 4). This absorption shifts to higher frequency (shorter wavelength) as bond strength increases for isolated, chain, sheet, and framework tetrahedron structure. These shifts allow for detailed identification of the igneous silicates, including variations within the solid solution series.

3.1.3. *Quantitative Analysis of IR Spectra*

A key strength of mid-infrared spectroscopy for quantitative mineral mapping lies in the fact that mid-infrared spectra of mixtures are linear combinations of the individual components (Thomson and Salisbury, 1993; Ramsey, 1996; Feely and Christensen, 1999; Hamilton and Christensen, 2000). The mid-IR fundamental vibration bands have very high absorption coefficients and therefore much of the emitted energy only interacts with a single grain. When absorption coefficients are low, as is the case for overtone/combination bands, the energy is transmitted through numerous grains and the spectra become complex, non-linear combinations of the spectral properties of the mixture. The linear nature of the thermal spectral emission of mineral mixtures has been demonstrated experimentally in particulates for mixtures of up to five components (Thomson and Salisbury, 1993; Ramsey, 1996). In these experiments the mineral abundance could be quantitatively retrieved using linear deconvolution techniques to within 5% on average. The linear mixing of mineral components in rock spectra has also been confirmed (Feely and Christensen, 1999; Hamilton and Christensen, 2000; Wyatt *et al.*, 2001; Hamilton *et al.*, 2001), with retrieved mineral abundances that are accurate to 5–10% in laboratory spectra.

The successful determination of mineral composition and abundance is illustrated in Figure 6. Mineral composition and abundance were determined both spectroscopically and using traditional thin-section techniques for a suite of 96 igneous and metamorphic rocks (Feely and Christensen, 1999). The rocks were used in their original condition; no sample cutting, polishing, or powdering was performed, and weathered surfaces were observed where available to best simulate remote observations. Comparison of the mineral abundances determined spectroscopically with the petrographically estimated modes for each sample gave an excellent agreement using high-resolution data (Figure 6a). The spectroscopically determined compositions matched the petrologic results to within 8–14% for quartz, carbonates, feldspar, pyroxene, hornblende, micas, olivine, and garnets. These val-

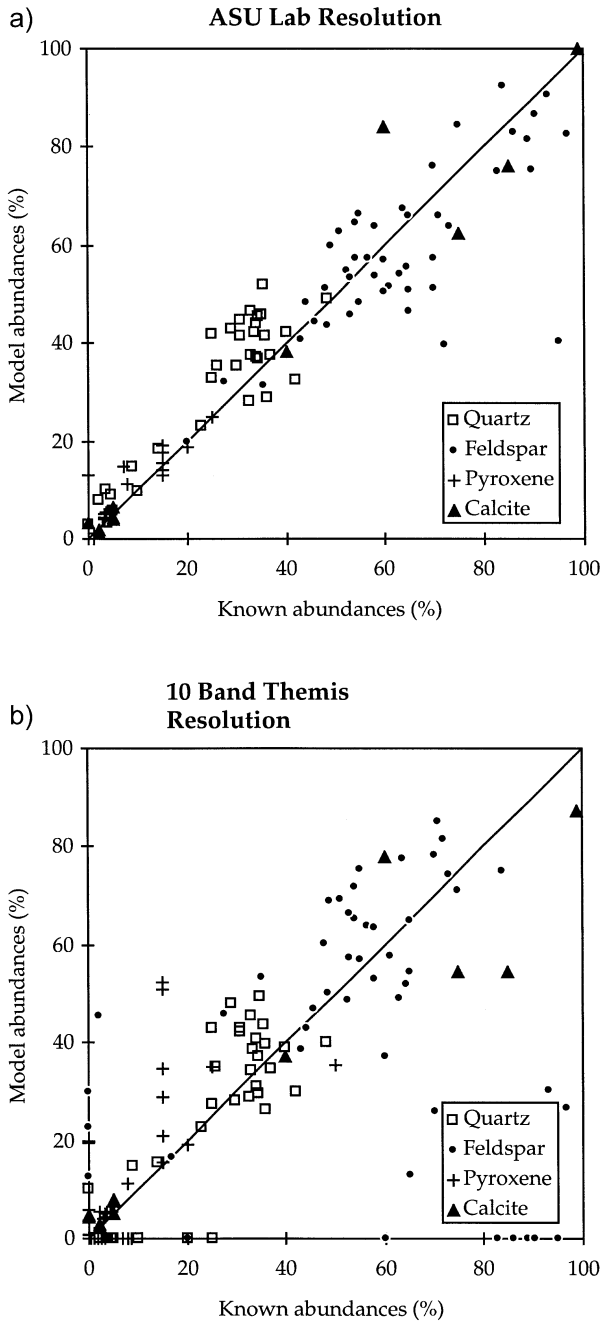

Figure 6. Quantitative mineral abundance determined from thermal-IR spectra. 'Known' abundances are derived from optical thin section measurements; 'model' abundances are derived from linear deconvolution of infrared spectral data (Feely and Christensen, 1999). The solid line corresponds to a perfect match between the two methods. (a) Mineral abundance derived from high spectral resolution (TES-like) data. (b) Mineral abundance derived from 10-band (THEMIS-like) data.

ues are comparable to the 5–15% errors typically quoted for traditional thin section estimates.

The mineral abundances derived using 10-band THEMIS-like resolution for the same hand sample rock suite are shown in Figure 6b. These results demonstrate that mineral abundance can be determined to within 15% using only 10 thermal-IR spectral bands on naturally-occurring rock surfaces. Similar results have been achieved for remotely-sensed aircraft observations on Earth through an atmosphere on a planetary surface (Ramsey *et al.*, 1999). Laboratory studies have also shown that a signal-to-noise ratio (SNR) of 35-100, corresponding to a noise-equivalent delta emissivity (NE$\Delta\varepsilon$) of 0.03 to 0.01, is sufficient to identify minerals using thermal-IR data (Feely and Christensen, 1999).

3.1.4. *Environmental Effects*

Variations in particle size and porosity produce variations in the spectra of materials at all wavelengths. Numerous quantitative models have been developed to investigate these effects (Vincent and Hunt, 1968; Hunt and Vincent, 1968; Conel, 1969; Hunt and Logan, 1972; Hapke, 1981, 1993; Salisbury and Eastes, 1985; Salisbury and Wald, 1992; Salisbury *et al.*, 1994; Moersch and Christensen, 1995; Wald and Salisbury, 1995; Mustard and Hays, 1997) and have demonstrated the importance of specular reflectance and scattering. Two basic behaviors are observed with decreasing grain size: (1) strong bands (high absorption) tend to get shallower; and (2) weak bands (low absorption) increase in contrast, but appear as emission maxima and reflectance minima (Vincent and Hunt, 1968).

Dust coatings and weathering rinds present a potential problem for any optical remotely-sensed measurements of Mars. However, the thickness of material through which sub-surface energy can escape increases linearly with wavelength. Thermal IR spectral measurements through coatings have been studied using mechanically deposited dust (Ramsey and Christensen, 1992; Johnson *et al.*, in press) and terrestrial desert varnish (Christensen and Harrison, 1993) as analogs to martian rock coatings. These results have shown that thermal-IR spectral observations can penetrate relatively thick (mean thickness up to $\sim 40-50$ μm) layers of these materials to reveal the composition of the underlying rock.

Atmospheric dust is also an issue in the remote sensing of the martian surface (Bandfield *et al.*, 2000b; Smith *et al.*, 2000; Christensen *et al.*, 2000b). However, scattering and absorption by fine-grained (< 5 μm) dust suspended in the atmosphere at typical opacities of < 0.2 (Smith *et al.*, 2001b, c) produces a linear contribution to the infrared spectrum (Smith *et al.*, 2000), and methods have been developed to quantitatively remove this contribution from THEMIS multi-spectral IR images (Smith *et al.*, 2000; Bandfield, 2002).

3.2. THERMAL INFRARED MULTI-SPECTRAL IMAGING

It has been established that minerals can be accurately identified in mixtures given high spectral resolution data, such as are available in a laboratory or from the MGS TES instrument (Ramsey and Christensen, 1998; Feely and Christensen, 1999; Hamilton, 1999; Christensen *et al.*, 2000b, c; Bandfield *et al.*, 2000a; Bandfield, 2002). The key question regarding the use of multi-spectral imaging is to determine what spectral resolution is sufficient to determine the presence and abundance of aqueous minerals. Thermal-infrared observations acquired in six spectral bands from 8 to 12 μm have proven extremely powerful for geologic mapping on Earth, and have clearly demonstrated that subtle differences in rock composition can be mapped (Gillespie *et al.*, 1984; Kahle *et al.*, 1980; Crisp *et al.*, 1990; Hook *et al.*, 1994; Edgett and Christensen, 1995; Kahle *et al.*, 1993; Ramsey, 1996).

The spectra of the key minerals shown in Figures 4 and 5 at TES spectral resolution are reproduced in Figure 7 at THEMIS resolution by convolving the laboratory spectra with the THEMIS filter response functions (see Section 4.2). Carbonates are identified using bands in calcite absorption (6.6 μm) and the continuum (7.5 μm) region. Silica (quartz) is also readily separated at this resolution from the other silicates, which have lower frequency absorptions. Key evaporite minerals, gypsum and apatite, also have well defined bands. Hydrated minerals (serpentine and clay) have unique absorption band shapes and positions, as do the common volcanic minerals, labradorite and augite, which have two very well defined absorptions in this spectral range.

Figure 8 provides an example of the rock composition mapping that can be achieved using broad-band multi-spectral thermal-IR data. This image was acquired using the 6-band Thermal Infrared Multispectral Scanner (TIMS) imager operating from 8–14 μm (Palluconi and Meeks, 1985) over the Granite Wash Mountains, Arizona. Three bands centered at $\sim$8, 9, and 10 μm are displayed in blue, green, and red, respectively. Different rock types are readily identified and their spatial distribution mapped using these thermal-IR multispectral data, as confirmed by detailed geologic mapping.

This image illustrates an important attribute of thermal-IR spectroscopy, where the spectra are sensitive to the major rock-forming minerals, rather than minor impurities, stains, and coatings. The 3-band data clearly discriminate carbonate (green), quartz-rich (red), and clay-rich (light blue), sedimentary rocks (purple/yellow), as well as basaltic (blue) and andesitic volcanic rocks (pink/purple). Soil surfaces of differing ages appear red to orange due to differing weathering processes that produce and remove clays and concentrate more resistant quartz-rich clasts over time.

The THEMIS 8-wavelength spectra will allow mineral identification and a quantitative determination of mineral abundance. The power of this combination of imagery and spectroscopy can be seen using spectra of rocks from the Granite Wash region convolved to the THEMIS surface-sensing bandpasses (Figure 9). Spectra

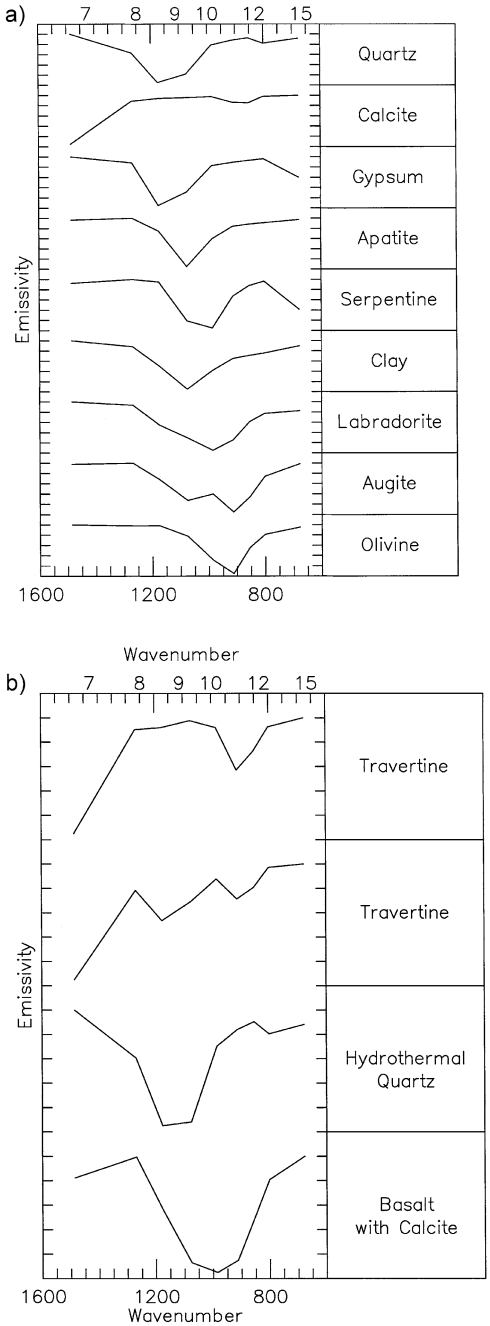

Figure 7. The emission spectra of key minerals at THEMIS spectral resolution. (a) The minerals from Figure 4 are shown at THEMIS resolution. The emissivity band depths vary from 0.2 to 0.4, well above the THEMIS noise level. (b) The hydrothermal rocks from Figure 5 are shown at THEMIS resolution.

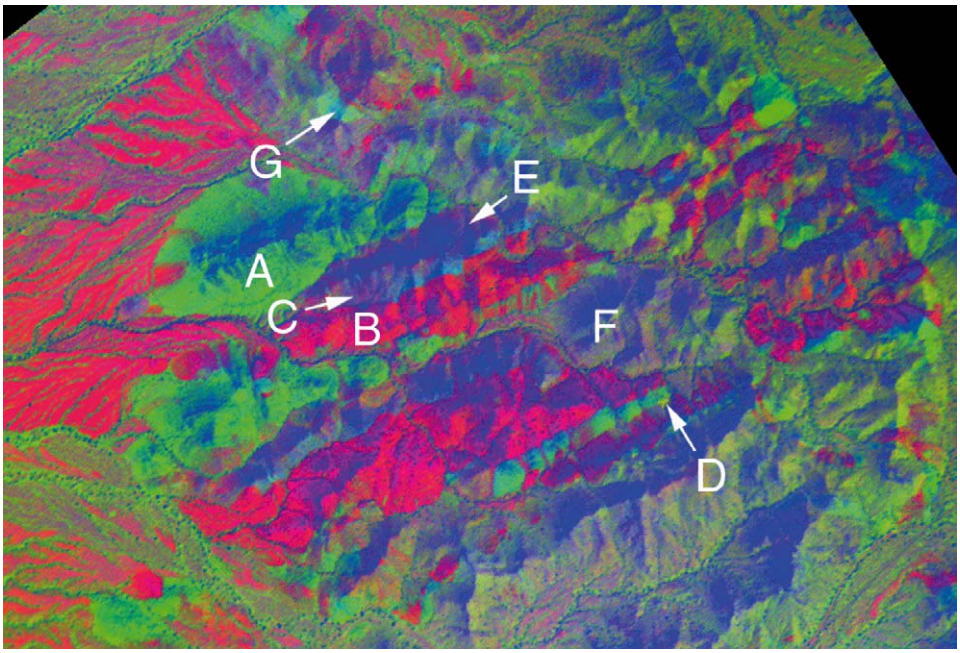

Figure 8. Infrared multispectral composition mapping. This three-band terrestrial IR image illustrates the rock and mineral discrimination using only three wavelength bands. Red surfaces are silica rich rocks and sediments, green units are carbonates, purple units are quartz-rich volcanic sediments, and blue units are mafic volcanics and metavolcanics. Also shown are the locations of the rock samples whose spectra are given in Figure 9.

were measured from unprepared, weathered and coated surfaces to duplicate remote measurements. The samples include fine-grained rocks with microcrystalline textures including those of hydrothermal origin, silica-rich rocks, quartzite, carbonate (limestone), a gypsum-rich soil, a hydrothermally altered basalt, and an ultra-mafic amphibolite.

The spectra of this suite of rocks at THEMIS resolution are unique and their mineral composition can be determined (Figure 9). Carbonates and quartz can be easily identified, as can gypsum, which appears bright yellow in the limited regions where it occurs in Figure 8. The sample of the microcrystalline quartz rock containing calcite veins has been hydrothermally altered and both carbonate and quartz are readily detected. The mafic rocks typical of expected martian volcanic rocks are distinct and easily separated from the aqueous samples.

The rocks in the Granite Wash image are heavily coated with desert varnish. These coatings are optically thick at visible wavelengths, with white sandstone appearing dark brown to black in the field.. However, as the Granite Wash image data demonstrate, the mid-infrared spectral signatures of the underlying rocks are identified through these coatings that are estimated to be up to 50 μm thick.

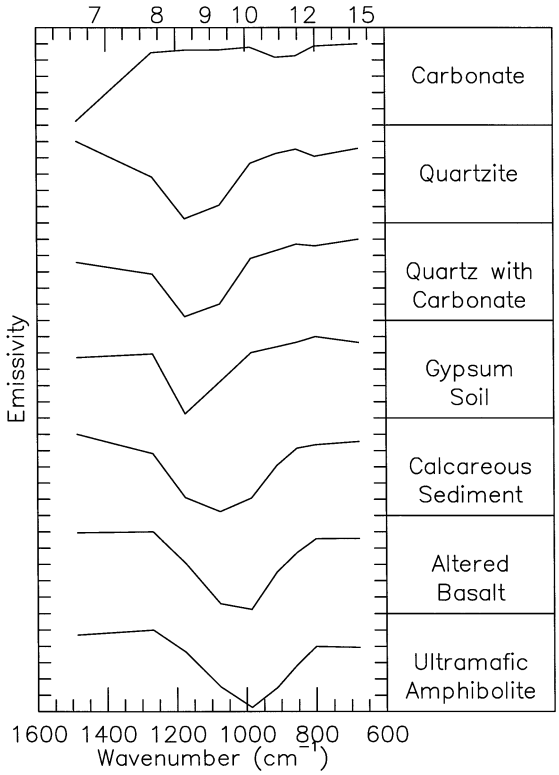

Figure 9. THEMIS simulated 8-band spectra of rock samples collected from the field sites shown in Figure 8. These spectra demonstrate the spectral discrimination possible with only 8 surface-sensing IR bands.

4. Instrumentation

4.1. Measurement requirements

THEMIS has two primary mission objectives: (1) to identify minerals and compositional units at 100-m spatial scales; and (2) to resolve surface features at scales significantly less than 100 m. The mineral mapping objective has three measurement requirements: (1) radiometric precision and accuracy necessary to resolve the expected band depths for minerals present at 10% abundance; (2) spectral resolution sufficient to identify key minerals; and (3) a spatial resolution sufficient to isolate small mineral deposits ($\sim$ 100 m). The morphology objective results in a measurement requirement of an instantaneous field of view (IFOV) that is a factor of 3–5 times less than 100 m.

The radiometric requirements are best stated relative to the band depth of minerals likely to be found on the martian surface weighted by their abundance. The band depth is defined here as the minimum emissivity in an absorption band relative to an emissivity of 1.0. The emissivity minima of particulates of the key

quartz and carbonate minerals are ~ 0.5 (band depth 0.5) in the 6–14 μm range; sulfates, phosphates, and clays are ~ 0.6 (band depth 0.4) ; typical volcanic minerals pyroxene, plagioclase, and olivine range from 0.7–0.8 (band depth 0.3–0.2). A surface containing carbonate grains at 10% abundance with an emissivity of 0.5 at 6.6 μm, mixed with 90% silicate with an emissivity of 1.0 would produce an absorption feature with an emissivity of 0.95. In order to observe this absorption feature, a noise equivalent delta emissivity (NE$\Delta\varepsilon$ of ~ 0.02 would be required. (Note that the signal-to-noise ratio (SNR) is the reciprocal of NE$\Delta\varepsilon$). The imaging nature of THEMIS will permit spatial aggregation of pixels and a spatial context to be developed, again increasing the acceptable noise level in each pixel (the detection of interesting sites will not depend on the occurrence of 10% carbonate in a single pixel). Near 10 μm where a number of minerals have absorption features, it is desired to have a higher NE$\Delta\varepsilon$ to allow mineral discrimination. Thus, the minimum NE$\Delta\varepsilon$ requirement for THEMIS is 0.02 (SNR = 50) in the 6.6 μm band and 0.007 (SNR = 143) in the 8–12.5 μm bands for each pixel.

The average local time of the THEMIS multi-spectral observations is 4:30 PM. The surface temperature follows the sub-solar point, but remains ≥ 245 K at this time over a wide latitude range for all thermal inertia surfaces (Kieffer *et al.*, 1977). For example, at 4:30 PM in southern hemisphere summer, the temperatures are between 245 and 270 from 45° S to 30° N, and in northern hemisphere summer the temperatures range from 235 to 250 K between 0° and 45° N. These latitude ranges encompass expected future rover/lander allowable ranges, and include 70% of the total surface area of Mars. A conservative requirement of a surface temperature of 245 K has been selected to set the instrument performance requirements.

The NE$\Delta\varepsilon$ requirement translates to a NEΔT requirement of 0.9 K at 7 μm and 0.5 K at 10 μm for a surface temperature of 245 K. The identification of nighttime temperature anomalies can be achieved with a NEΔT of 1 K at a typical nighttime surface temperature of 180 K.

4.2. General description

The design of the THEMIS is intentionally conservative. We have adopted a multispectral, rather than hyperspectral, approach that is sufficient to quantitatively determine mineralogy and allows global coverage within the available data volume. The THEMIS flight instrument, shown in Figure 10, consists of infrared and visible multi-spectral imagers that share the optics and housing but have independent power and data interfaces to the spacecraft to provide system redundancy. The details of the instrument design are given in Table 1. The telescope is a three-mirror anastigmat with a 12-cm effective aperture and a speed of f/1.6. A calibration flag, the only moving part in the instrument, provides thermal calibration and is used to protect the detectors from direct illumination from the Sun. The electronics provide digital data collection and processing as well as the instrument control and data

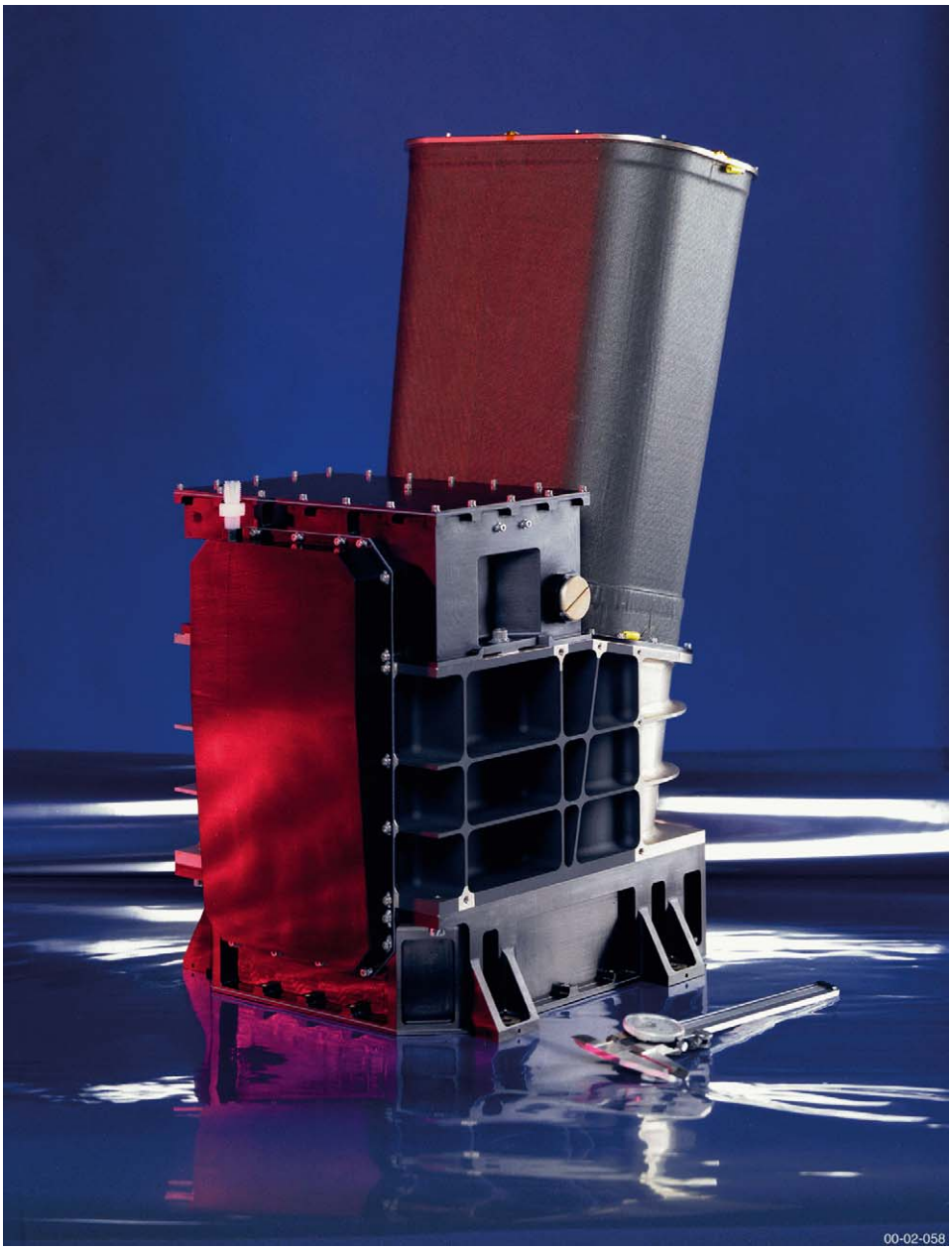

Figure 10. THEMIS flight instrument.

TABLE I

Themis instrument design summary

Quantities to be measured:	Emitted radiance in 10 ∼1-μm bands (9 different wavelengths) centered between 6.8 and 14.9 μm at 100 m per pixel spatial resolution
	Solar reflected energy in 5 ∼50 nm bands centered from 0.42 to 0.86 μm at 18 m per pixel spatial resolution
Detectors:	Multi-spectral IR imager: 320 × 240 element uncooled microbolometer array
	Visible imager: 1, 024 × 1, 024 element silicon array
Expected performance:	NE$\Delta\varepsilon$ @ 245 K & 10 μm = 0.005.
	NEΔT @ 245 K & 10 μm = 0.5 K.
	NEΔT @ 180 K = 1 K.
	SNR > 100 in visible imager at 0.25 albedo, 60° solar incidence angle
Optical/Mechanical Design:	12-cm effective aperture f/1.6 telescope to view nadir shared by multi-spectral IR and visible imagers. Internal calibration flag provides calibration and Sun avoidance protection functions. IR spectrometer is 10-strip filter pushbroom design with time delay integration. Visible multi-spectral imager is 5-strip filter frame-scan design.
Fields of View:	IR imager has a 4.6° (80 mrad) cross-track by 3.5° (60 mrad) down-track FOV with a 0.25 mrad (100 m) IFOV at nadir.
	Visible imager has a 2.66° (46.4 mrad) cross-track by 2.64° (46.1 mrad) down-track FOV with 0.045 mrad (18 m) IFOV in 1024 × 1024 pixels at nadir. The two imagers are spatially bore-sighted.
In-Flight Calibration:	Periodic views of an internal calibration flag.
Thermal Requirements:	Operating range −30 °C to +30 °C. Non-operating range −30 °C to +45 °C. No detector cooling required.
Digital Data	8-bit delta radiance in IR imager
	8-bit radiance in visible imager
Data rate:	IR imager has instantaneous internal rate of 1.17 Mbits/sec. Data rate to spacecraft after real-time compression is 0.6 Mbits/sec.
	Visible imager has instantaneous internal rate of up to 6.2 Mbits/sec. Data rate to spacecraft is < 1.0 Mbits/sec. 4 Mbyte RAM internal data buffer for data processing and buffering for delayed output to spacecraft.
On-board Data Processing:	IR imager: Gain and offset; time delay integration, and data compression in electronics; data formatting using spacecraft computer.
	Visible imager: Lossless and predictive compression in firmware; selective readout and pixel summing on spacecraft.
Solar Protection:	Provided by calibration flag in stowed position.
Mass:	11.2 kg
Size:	29 cm by 37 cm by 55 cm
Power:	14 W orbital average

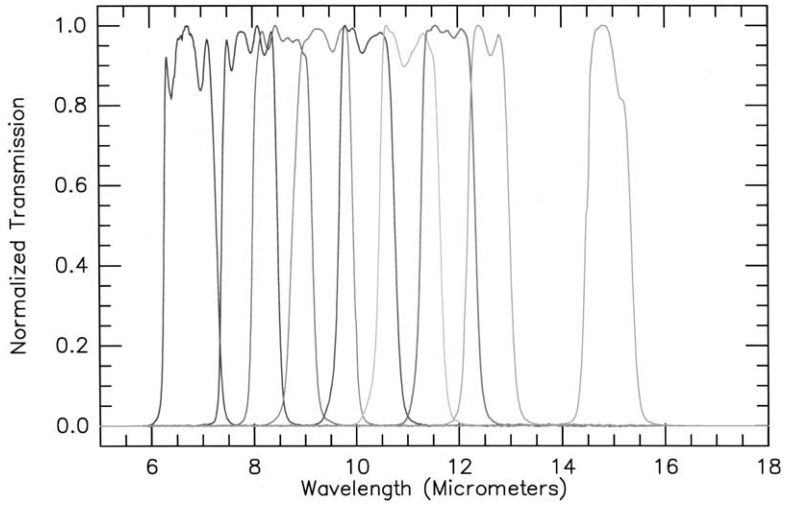

Figure 11. THEMIS IR imager spectral bandpasses. Data were collected at SBRS prior to instrument delivery to the spacecraft.

interface to the spacecraft. The instrument weighs 11.2 kg, is 29 cm by 37 cm by 55 cm in size, and consumes an orbital average power of 14 W.

A major feature of the instrument is the use of an uncooled microbolometer array operated at ambient temperature, which substantially reduced the complexity of instrument fabrication, testing, spacecraft interfaces, and mission operations. This array has 320 cross-track pixels and 240 down-track pixels with an IFOV of 100 m and an image width of ~ 32 km. A small thermal electric (TE) cooler is used to stabilize the IR focal plane temperature to ± 0.001 K. The IR imager has ten stripe filters that produce ten ~ 1-μm wide bands at nine separate wavelengths from 6.78 to 14.88 μm (Table 2; Figure 11). Two filters (Bands 1 and 2) cover the same spectral region centered at 6.78 μ to improve the detection of carbonate by improving the signal to noise in this spectral region. The nine IR wavelengths include eight surface-sensing wavelengths (Bands 1–9) and one atmospheric wavelength (Band 10).

The visible imager is a derivative of the Malin Space Science Systems (MSSS) Mars Polar Lander Mars Decent Imager (MARDI), with a 5-filter subset of the MSSS Mars Color Imager (MARCI) developed for the Mars Climate Orbiter. It has 1,024 cross-track pixels with an 18-m IFOV covering a 18.4-km swath boresighted with the IR imager through a beamsplitter. The visible imager has five stripe filters centered from 0.425 to 0.86 μm (Table 3; Figure 12).

4.3. Optical design

In order to integrate the visible and IR bands into a single telescope, a fast, wide field-of-view reflective telescope has been used. The 3.5° (down-track) $\times$ 4.6°

TABLE II
THEMIS infrared band characteristics

Band	Center Wavelength (μm)	Half Power Point – Short Wavelength (μm)	Half Power Point – Long Wavelength (μm)	Band Width (Full Width Half Max) (μm)	SNR
1	6.78	6.27	7.28	1.01	33
2	6.78	6.27	7.28	1.01	34
3	7.93	7.38	8.47	1.09	104
4	8.56	7.98	9.14	1.16	163
5	9.35	8.75	9.95	1.20	186
6	10.21	9.66	10.76	1.10	179
7	11.04	10.45	11.64	1.19	193
8	11.79	11.26	12.33	1.07	171
9	12.57	12.17	12.98	0.81	132
10	14.88	14.45	15.32	0.87	128

(cross-track) field of view is achieved with a 3 mirror f/1.6 anastigmat telescope with an effective aperture of 12 cm and a 20-cm effective focal length. The design allows for excellent baffling to minimize scattered light. It is based on a diamond-

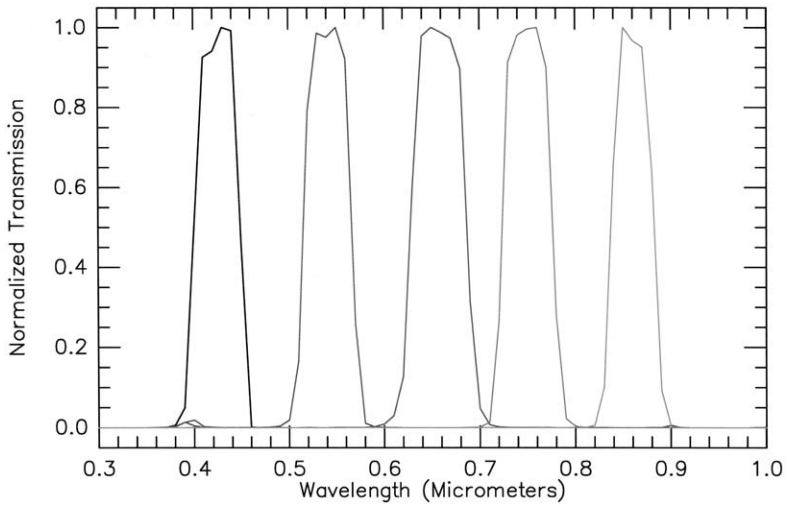

Figure 12. THEMIS visible imager spectral bandpasses. Data were collected at MSSS prior to visible sensor delivery to SBRS.

TABLE III
THEMIS visible band characteristics

Band	Center Wavelength (μm)	Half Power Point – Short Wavelength (μm)	Half Power Point – Long Wavelength (μm)	Bandwidth (Full Width Half Power) (μm)
1	0.425	0.400	0.449	0.049
2	0.540	0.515	0.566	0.051
3	0.654	0.628	0.686	0.053
4	0.749	0.723	0.776	0.053
5	0.860	0.837	0.882	0.045

turned bolt-together approach to telescope design, fabrication, alignment and test. A telescope ray trace is shown in Figure 13.

The system was optimized to match the high signal performance required for the IR imager and the spatial resolution needed for the visible camera. The 9-μm pitch of the visible array maps to a ground sample distance (GSD) of 18 meters with an MTF of approximately 0.1 at Nyquist. Similarly, the 50 μm pitch of the IR focal plane array maps to a GSD of 100 M.

A major aspect of THEMIS is the use of diamond-turned 'bolt-together' telescope technology. The telescope development used design and analysis techniques that allowed complex off-axis designs to be fully modeled. The manufacture utilized high-precision machining capabilities that allowed the entire optical stage to be machined and assembled without manual optical component adjustments, and achieved diffraction-limited performance in both the visible and infrared. Specified mounting surfaces were machined with extremely tight tolerances ($\pm$ 0.0002 in). The optical surfaces were machined directly from high order aspheric equations. The telescope was manufactured with aluminum to reduce cost and is significantly light-weighted. Nickel plating and automated post polishing were used to keep the surface scatter to levels unobtainable with conventional diamond turning techniques.

4.4. Focal plane assemblies

THEMIS uses uncooled microbolometer detector arrays that have been recently declassified and were produced commercially by the Raytheon Santa Barbara Research Center (SBRC) under license from Honeywell, Inc. The THEMIS IR imager design is based on a Raytheon hand-held imager developed for rugged military use, thus significantly reducing the development cost of the IR focal plane assembly. The microbolometer array contains 320 pixels cross track by 240 pixels along

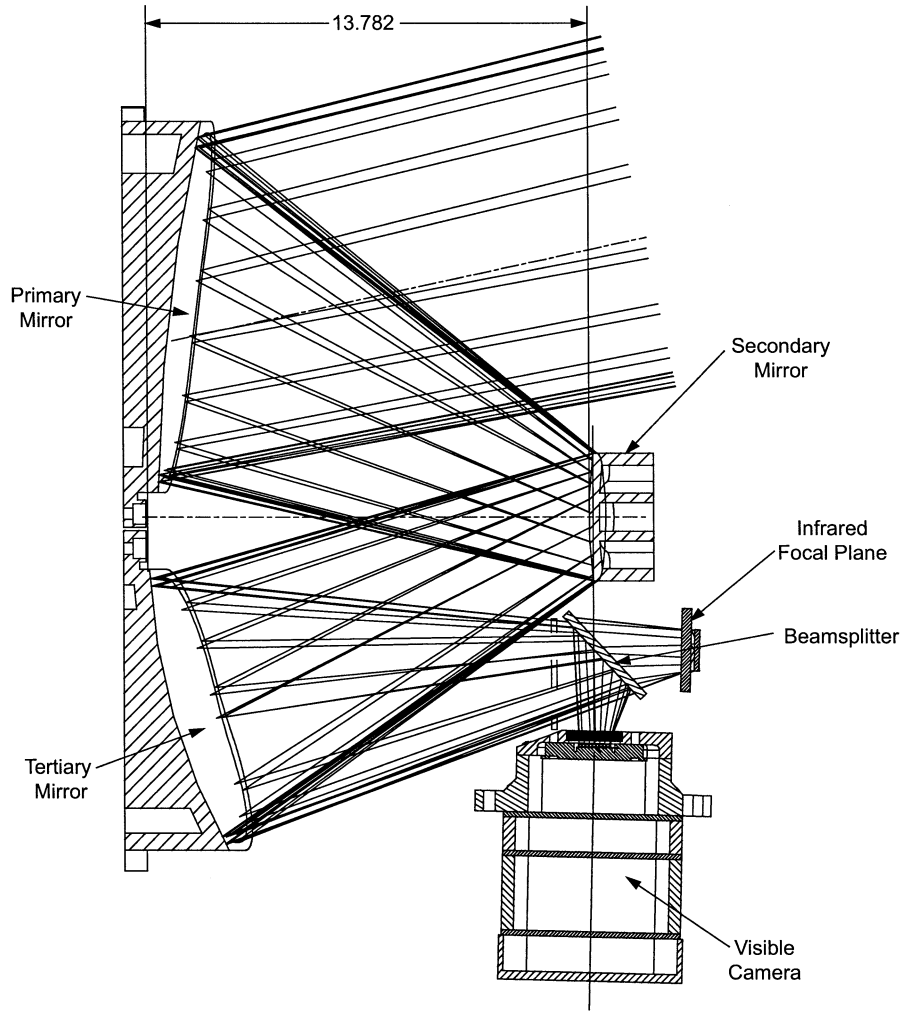

Figure 13. The THEMIS optical schematic and raytrace.

track, with a square 50 micron pixel pitch. The microbolometer arrays were grown directly on the surface of Readout Integrated Circuits (ROIC) which are designed by SBRC and utilize custom Digital Signal Processing electronics.

Spectral discrimination in the infrared is achieved with ten narrowband stripe filters. Each filter covers 16 lines in the along track direction with an 8-line 'dead-space' between filters. To maximize manufacturing yield and reduce costs, the stripe filters were fabricated as separate stripe filters butted together on the focal plane as shown in Figure 14. The THEMIS arrays and filters are mounted within a dewar assembly that seals the arrays and allows for simplified ambient testing. The along-track detectors under a common spectral filter are combined by the use of time-delay and integration (TDI) to improve the instrument's signal-to-noise

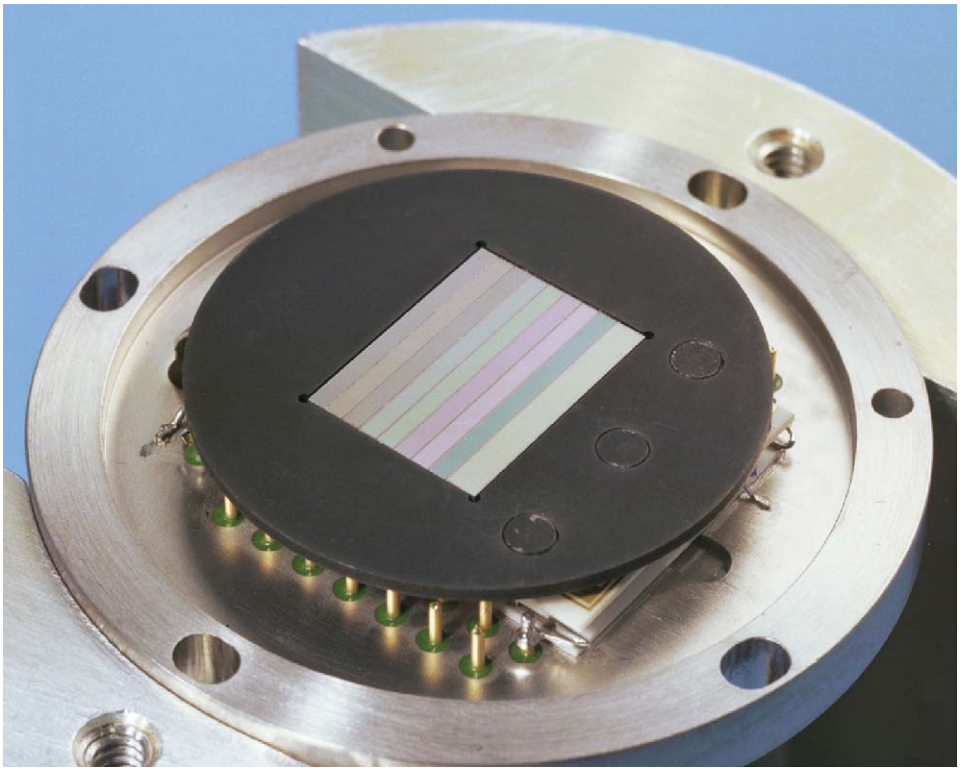

Figure 14. The THEMIS infrared focal-plane and stripe-filter layout.

performance. The calculated dwell time for a single pixel, at a martian orbit of 400 km and a 100-meter footprint is 29.9 msec, which closely matches the 30 Hz frame rate for the standard microbolometer.

The visible camera supplied by MSSS consists of a small ($5.5 \times 8.5 \times 6.5$ cm, < 500 gm) unit incorporating a focal plane assembly with five color filters superimposed on the CCD detector, a timing board, a data acquisition subsystem and a power supply. This sensor utilizes a Kodak KAI-1001 CCD that was flown in the MS'98 MARDI instrument. This detector has 1024×1024 9-micrometer pixels (1018×1008 photoactive). The visible imager uses a filter plate mounted directly over the area-array detector on the focal plane. On the plate are multiple narrowband filter strips, each covering the entire cross-track width of the detector but only a fraction of the along-track portion of the detector. This sensor uses a 5-filter subset of the 10-filter MS'98 MARCI wide angle camera to acquire multispectral coverage. Band selection is accomplished by selectively reading out only part of the resulting frame for transmission to the spacecraft computer. The imager uses 5 stripes each 192 pixels in along-track extent. The entire detector is read out every 1.3 seconds. The five bands selected are centered near 425, 550, 650, 750, and 860 nm (Figure 12)

4.5. ELECTRONICS DESIGN

Both the visible and infrared cameras utilize commercial off-the-shelf electronics with modifications to accommodate space environmental requirements. Dedicated, miniaturized electronics provide ultra-stable, low-noise clock and bias signals to the focal planes, stabilize IR focal plane temperature within ± 0.001 °C, and perform analog and digital processing of the output signals.

The IR signal change begins at the focal plane that generates an analog output. An initial 8-bit analog DC offset correction occurs on the focal plane, followed by analog-to-digital conversion to 12-bit words, which are then corrected for gain and offsets. This correction is provided by the electronics of the IR camera and consists of a 12-bit fine offset and 8-bit gain and responsivity adjustment, performed in real time on a pixel-by-pixel basis. This process eliminates all of the significant noise elements with the exception of the fundamental random noise term. The output from this processing is an 8-bit word for each pixel.

The spacecraft interface electronics supply final processing of the focal plane data, a data and command interface to the spacecraft, and overall instrument power conditioning. Internal THEMIS data processing in firmware includes 16:1 TDI processing and lossless data compression for the IR bands using a hardware Rice data compression algorithm chip. The bulk of the interface electronics is performed using Actel Field Programmable Gate Arrays (FPGAs), that are packaged using a mixture of conventional and Sealed Chip-On-Board, High-Density Multiple Interconnect technology and chip stack memory. The visible and IR subsystems have independent power supplies, the IR power supply uses off-the-shelf modules and requires only a few discrete components for input filtering to assure electromagnetic compatibility with the rest of the spacecraft. The spacecraft processor performs final data stream formatting for both the IR and the visible data.

The visible sensor requires 7 clock signals: a two-phase vertical clock (V1/V2), a two-phase horizontal clock (H1/H2), a sub-state clear clock (S), a reset clock (R), and a fast- dump clock (F). In addition, the ADC requires a convert clock.

The amplified CCD signal is digitized by an Analog Devices AD1672 12-bit ADC running at its maximum rate of 3 MSPS. For each pixel, both reset and video levels are digitized and then subtracted in the digital domain to perform correlated double sampling (CDS).

The digital electronics are responsible for clock generation, sampling of the CCD signal, conversion of the 12-bit samples to 8-bit encoded pixels, storage of the pixels, and finally readout of the pixels to the spacecraft. The zero reference ('reset') level for each pixel is digitized and stored in a register. The sum of the video plus zero reference ('video') level is then digitized, and an arithmetic subtraction is performed to produce the final result. The CCD output only requires scaling to the ADC range; no analog sampling, delay or differencing is required. The digital signal processor within the visible sensor generates the CCD clocks, reads the reset and video levels from the ADC, performs the correlated double

sampling subtraction, reduces the pixel from 12 to 8 bits, applies optional 2×2 or 4×4 pixel summinglossless (2:1) first-difference Huffman compression, and transmits it digitally over the serial communication interface to the spacecraft CPU.

4.6. MECHANICAL DESIGN

The THEMIS main frame is composed of aluminum and provides the mounting interface to the spacecraft as well as the telescope assembly, thermal blankets, and thermal control surface. The focal plane assemblies are mounted in the main frame using brackets that provide for the necessary degrees of freedom for alignment to the telescope. The calibration shutter flag is stored against a side wall that will maintain a known temperature of the flag for calibration purposes. Aluminum covers are installed over the electronics circuit cards to provide EMI, RFI, and radiation shielding as required. There is no reliance on the spacecraft for thermal control of THEMIS, other than the application of replacement heater power when the instrument is off. The thermal control plan includes the use of multi-layer insulation blankets and appropriate thermal control surfaces to provide a stable thermal environment and a heatsink for the electronics and the TE temperature controller on the focal plane arrays.

4.7. PERFORMANCE CHARACTERISTICS

The THEMIS IR performance was estimated in the design phase using expected performance values for the IR focal plane, filters, optical elements, TDI, and electronics. The following equations define the parameters used to predict the noise equivalent delta emissivity (NE$\Delta\varepsilon$):

$$\mathrm{NE}\Delta\varepsilon = \frac{\mathrm{NEP}}{\mathrm{P}^{*}_{sc}\sqrt{\mathrm{n}_{\mathrm{TDI}}}}$$

where

NEP = Noise equivalent power

P_{sc} = scene power incident in the bolometer

$\mathrm{n}_{\mathrm{TDI}}$ = number of samples in TDI (16)

$$\mathrm{NEP} = \frac{\mathrm{V}_{\mathrm{nz}}}{\mathrm{R}}$$

where

V_{nz} = noise voltage in volts

R = bolometer responsivity in volts/mW

NEP for the microbolometer is a constant in this analysis for two reasons: (1) bolometer noise is not a function of photon flux (as it is for photon-limited

PV detectors where the shot noise component of the flux dominates); and (2) the responsivity of the bolometer over wavelength is taken as constant and based on that measured in the 'flat' portion of the spectral curve for the bolometer.

The detector output is based on the Mars scene temperature, instrument parameters, and predicted bolometer performance. The radiance calculation is based on Planck's law, multiplied by the optics solid angle (omega) for an average f1.6 system, the area of the microbolometer, the overall optics transmission, and the spectral response predicted for the microbolometer. The resulting power is then divided into the NEP, and improved by the square root of the number of samples in TDI, to yield the NE$\Delta\varepsilon$ ratio. SNR is the reciprocal of this NE$\Delta\varepsilon$. The scene power incident on the bolometer in mW (Psc) is:

$$P_{sc} = L(T_{sc}, l_{sc})^* A_{det}{}^* \Delta_l^* T_{opt}{}^* T_{filt}{}^* T_{bol}(l_s c)^* \Omega$$

Where the radiance at instrument aperture (L) in mW/cm^2-μm-sr is given by:

$$L(T_{sc}, l_{sc}) = \frac{c_1}{l_{sc}^5}{}^* \frac{1}{e^{c_2/l_{sc}T_{sc}} - 1}{}^* 1000$$

and

$l_{sc} =$ peak wavelength in μm

$T_{sc} =$ scene temperature in °K

$c_1 = 2\pi hc^2 = 37415$ W-μm/cm^4

$c_2 =$ ch/k $= 14388$ μm $-^\circ$ K

$A_{det} =$ detector area in cm^2

$\Delta_l =$ bandwidth of the stripe filters in μm

$T_{opt}{}^* T_{filt} =$ combined optics and filter transmission

$T_{bol} =$ predicted spectral response of the bolometer

$\Omega =$ optics solid angle in sr

The predicted performance for the infrared bands produced NE$\Delta\varepsilon$'s ranging from 0.007 to 0.038 when viewing Mars at surface temperatures of 245K to 270 K.

The measured noise equivalent spectral radiance (NESR) values are given in Figure 15. The measured SNR for a reference surface temperature of 245 K is summarized for each band in Table 3. Most of the variation in SNR between bands is due to the variation in emitted energy for the 245 K reference temperature. As seen from these results, the THEMIS IR imager exceeds the proposed measurement requirements by a factor of two in most bands.

Signal-to-noise ratios for the visible imager were computed for a low albedo (0.25), flat-lying surface viewed at an incidence angle of 67.5° under aphelion conditions. The SNR values for this case vary from 200 to 400.

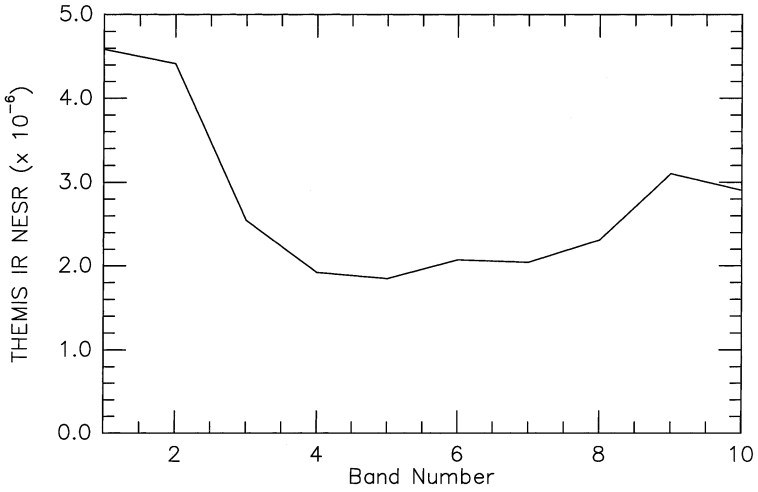

Figure 15. Noise equivalent spectral radiance (NESR) for the 10 THEMIS IR bands. Units are W cm^{-2} μm^{-1} sr^{-1}.

4.8. SOFTWARE

The flight software for the IR imager resides on the spacecraft computer and performs the formatting and data packetization. Instrument commanding is done using discrete spacecraft commands to the THEMIS instrument over an RS-422232 synchronous serial command line. These commands consist of: (1) IR camera on/off/stand-by; (2) visible camera on/off/stand-by; (3) calibration flag shutter control and electronics synchronization; and (4) instrument parameter settings (gain, offset, integration time, etc).

The visible imager software runs on two processors: the main spacecraft CPU and the internal digital signal processor (DSP). The CPU is responsible for instrument operational commands and image post- processing and compression. The DSP is responsible for generating the CCD clocks, emulating the required analog processing and transmitting the data output to the CPU.

The algorithm employed compresses each image line independently by encoding first differences with a single, fixed Huffman table. Selective readout and pixel summing can also be performed by the DSP softwreare. Experience has shown that the volume of data likely to be returned from a spacecraft often evolves during a mission. Implementing data compression in software on the spacecraft computer provides the maximum flexibility for the science and spacecraft team to tradeoff data return and buffer space usage. Two compression modes were developed for the VIS: a fast lossless predictive compressor, and a slower lossy discrete cosine transform compressor. Both forms are applied by the spacecraft CPU using THEMIS-provided software. The lossless algorithm compresses each image line independently by encoding pixel first differences with a single, fixed Huffman table.

5. Mission Operations

5.1. Overview

The Mars Odyssey spacecraft is in a near-polar sun synchronous orbit with an approximately 4:30 PM equator-crossing local time. From this orbit the THEMIS infrared imager will image 100% of the planet both day and night. In addition, THEMIS will be used for selective targeting throughout the mission for regions of high-interest identified from TES, MOC, THEMIS, or other experiments.

Collection of THEMIS IR and visible data is flexible, based on scientific priorities, observing conditions, and data rates. Optimal observing conditions for IR mineralogic mapping occur during mission phases where the local true solar time is the earliest in the afternoon, and when the atmosphere has the lowest dust and water-ice opacity. Optimal conditions for visible imaging occur when the incidence angles are between 60 and 80°. Nighttime images can be acquired during all phases of the mission, but will be emphasized when the daytime IR images are of lower quality. Polar observations will be acquired through the martian year to observed all aspects of autumn cap growth, winter night, and spring retreat.

5.2. Image collection

THEMIS IR images are acquired at selectable image lengths, in multiples of 256 lines (25.6 km). The image width is 320 pixels (32 km from the nominal mapping orbit) and the length is variable, as given by ((# frames) * 256 lines) - 240. The allowable number of frames varies from 2 to 256, giving minimum and maximum image lengths of 272 and 65,296 lines respectively (27.2 km and 6,530 km from the nominal mapping orbit). The bands returned to the ground are selectable. THEMIS visible images can be acquired simultaneously with IR images, but the spacecraft can only transfer data from one of the two THEMIS imagers at a time. The IR image transfers data as it is being collected, while the visible images are stored within an internal THEMIS buffer for later transfer to the spacecraft computer.

The visible images are acquired in framelets that are 1024 samples crosstrack by 192 lines downtrack in size. Framelets are typically taken at 1-sec intervals, resulting in 26 rows of downtrack overlap at a nominal orbit velocity of 3.0 km/sec. Images can be composed of any selectable combination of bands, image length, and integer pixel summing that can be stored within 3.734 Mbytes THEMIS internal buffer. The size of an image is given by:

$$[(1024^{*}192)^{*}\#\text{framelets}^{*}\#\text{bands}]/[\text{summing}^{2}] = 3.734 \text{ Mbytes}$$

Thus, for example, with no summing either a single-band, 19-framelet ($\sim$60 km) image or a 5-band 3-framelet (8.5 km) image can be collected.

THEMIS images are calibrated using periodic views of the internal calibration flag together with an instrument response function determined pre-launch. The flag

is closed, imaged, and reopened at selectable intervals throughout each orbit. This process produces gores in the surface observation lasting approximately 50 seconds for each calibration. Calibration data typically are acquired at the beginning and end of each image, but can be spaced to meet the calibration accuracy requirements, while minimizing the loss of surface observations.

5.3. DATA ALLOCATION

THEMIS data collection will be distributed between the mineralogic, temperature, and morphologic science objectives in both targeted and global mapping modes. A baseline observing plan has been developed to prioritize the total data volume returned by THEMIS between the different objectives. This plan devotes 62% of the total data to the IR imager and 38% to the visible, averaged over the course of the Primary Mission. In the baseline plan the IR data will be further sub-divided into 9-wavelength daytime mineralogic observations (47% of total data return) and 3-wavelength nighttime and polar temperature mapping (15% of total data). The visible data will be sub-divided into panchromatic images (37% of total data) and 5-band multi-spectral images (2%). In this example we have assumed a lossless data compression factor of 1.7 for the IR imager and a combination of lossless (40%), and lossy with compression factors of 4× (30%) and 6× (30%) for the visible imager. With these allocations THEMIS will fully map Mars in daytime IR and will map the planet 1.5 times in nighttime IR. The visible imaging will cover $\sim 60\%$ of the planet at 18-m resolution in one band (50,000 18 × 60km frames) and $< 1\%$ in 5-band color. Tradeoffs between monochromatic and multi-spectra imaging, as well as variations in the degree of lossy compression and pixel summing, will be made to maximize the science return from the visible imager.

5.4. FLIGHT OPERATIONS

The THEMIS instrument is operated from ASU, building on the facility and staff developed and in place for the MGS TES investigation. No special spacecraft operation or orientation is required to obtain nominal THEMIS data. The instrument alternates between data collection (≤ 3.5 hours per day) and idle modes based on available Deep Space Network (DSN) downlink rates. These modes will fall within the allocated resources (e.g. power), and do not require power cycling of the instrument. All instrument commands are generated at ASU, delivered electronically to the Mars Odyssey Project, and transmitted to the spacecraft. Data are retrieved from the mission database and stored at ASU, where the health and welfare of the instrument are monitored, the data are processed and calibrated, and the archive database is created and stored.

6. Data Reduction and Validation

6.1. Overview

The data received on the ground are in the form of compressed, scaled, 8-bit 'data numbers' (DN) that represent the delta signal between the scene and the internal reference calibration flag. Data processing consists of decompression, radiometric calibration, and systematic noise removal. For the final generation of geometrically corrected, map-projected data products, each image is processed independently and multiple images can be concatenated together into mosaics. Distortions caused by optics and spacecraft motion are removed concurrently with map projection to avoid multiple resampling degradation.

6.2. Data calibration

The THEMIS instrument was radiometrically, spectrally, and spatially calibrated prior to delivery. Three categories of calibration were performed: (1) spatial calibration; (2) spectral calibration; and (3) radiometric calibration including the absolute radiometry, the relative precision (SNR), and the calibration stability during an image collection. The data returned from the instrument in-flight are converted to scene radiance by: (1) adjusting for the gain and offset that were applied in the instrument to optimize the dynamic range and signal resolution for each scene; (2) correcting for drift or offset that occur between observations of the calibration flag; and (3) converting signal to radiance using the instrument response functions determined prior to instrument delivery using a thermal vacuum chamber at the SBRS facility.

Calibration data for the IR sensor were collected at five instrument temperatures (-30, -15, 0, 15, and 30 °C) and seven target temperatures (170, 190, 210, 247, 262, 292, and 307 K). These temperatures were chosen to cover the range of operating and scene temperatures expected at Mars. A full-aperture, calibrated blackbody was placed inside the vacuum chamber and viewed directly by the THEMIS instrument. This blackbody was developed for the SBRS Moderate resolution Imaging Spectrometer (MODIS) instrument, and is a calibrated source traceable to NIST standards with an uncertainty of ± 0.032 K (one sigma). Included in this assessment is a temperature uniformity of 0.020 K, a stability of 0.010 K and an emittance 0.99995 ± 0.00005 (Young, 1999b, c).

For each calibration data set the instrument and blackbody were temperature stabilized at < 0.1 °C. Observations were acquired of the THEMIS internal calibration flag immediately before the collection of a set of calibration images. A 10-sec image was acquired for each point in a matrix of five different gains with five offsets (25 images total) that cover the range of values to be used at Mars. At the completion of this series of images, the calibration flag was reimaged to determine any temperature drift or offset that occurred. The calibration data were adjusted for these minor changes.

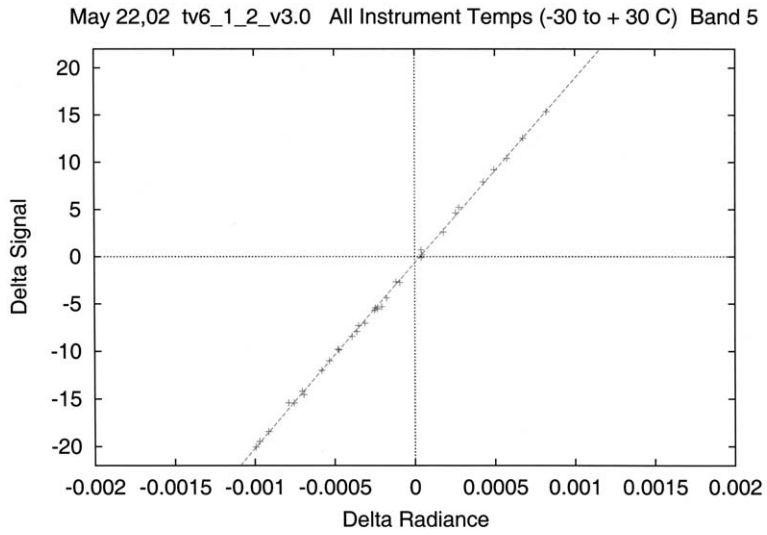

Figure 16. IR imager instrument response function. Example is for Band 5. Radiance units are W cm^{-2} μm^{-1} sr^{-1}.

The response function was computed for each band using the measured output signal versus the computed blackbody radiances. The instrument firmware automatically sets the signal level when viewing the internal calibration flag to 128 DN for a gain of 1, offset of 0. Scene signals are measured relative this value, with the appropriate gain and offset terms applied. As a result, targets colder than the flag have signal DNs (gain and offset removed) <128, whereas warmer scenes have a DN>128.

Figure 16 shows an example of the resulting delta signal (scene-flag; gain = 1, offset = 0) versus delta radiance for Band 5 for all 35 calibration set points. This figure also shows the best-fit linear function that will be used to convert DN to radiance for the Mars data. The measured response values are linear and show no instrument temperature effects. The best-fit response function does not pass through the origin because of the fact that the view of the calibration flag does not include the slightly absorbing fore-optics. Thus, the delta-signal appears slightly negative (less apparent energy) when viewing a scene at the same temperature as the flag. Because the function shown in Figure 16 will be used in flight, this effect is exactly reversible and will not result in any systematic errors in the Mars observations.

The radiometric calibration accuracy of the IR imager is expected to be within $\pm 5\%$; the relative spectral calibration will be to within $\pm 3\%$, which is well within the calibration requirements for mineral spectral analysis.

The THEMIS visible sensor was calibrated over temperature under vacuum by viewing an external calibrated integrating sphere. This sphere was developed for the SBRS Landsat program and is calibrated to a NIST standard with a 1 sigma

accuracy of 3.5%. Short term stability is maintained at less than 1% over 14 days (Young, 1999a). Overall uniformity of illumination is better than 0.25% (Young, 1999a).

The visible response function was calculated using a linear fit to the measured signal, with dark current removed, versus calibrated lamp radiance. The measured visible filter functions were integrated over the measured lamp output spectra to produce band-integrated signal versus radiance functions.

6.3. Standard data processing

Ground data processing consists of a series of steps that include: depacketization, decompression, instrument health monitoring, radiance calibration, long-term performance monitoring, standard product generation, data quality verification, data archiving and distribution, and preliminary science analysis. These steps must be performed at a rate designed to keep pace with the collection of data by the instrument. The IR data are calibrated to radiance, derived surface kinetic temperature and spectral emissivity, and atmospheric temperature. Geologic processing proceeds with mapping of spectral components, comparison of spectral emissivity with a spectral library, component identification, and identification of temperature anomalies.

6.4. Data archiving

Data will be accumulated and archived routinely during standard mission operations as described in the Mars 2001 Odyssey Project Data Archive Plan. All products generated will conform to the standards developed for the Planetary Data System. Data validation and archiving will be performed at ASU. Standard products will consist of images of calibrated radiance in the IR and visible, surface brightness temperature, and atmospheric brightness temperature.

7. Education/outreach

THEMIS investigation builds on the TES Arizona Mars K-12 Education Program, which has over 10 years experience doing highly-leveraged education outreach for Mar Observer and MGS (Edgett, 1995; Edgett and Rice, 1995; Edgett and Christensen, 1996; Edgett *et al.*, 1997). Activities have included: student visits to MGS TES facility; biannual teacher workshops; field trips; workshops at national, regional, and state teacher conferences; visits to schools, community, senior, and science centers; annual teacher guides; lithographs; Spanish material; WWW site; a quarterly newsletter; and a quarterly, age-appropriate, National Standards-based resource for K-8 children.

A major element of the THEMIS outreach program is the THEMIS Student Imaging Project. The objective of this program is to give students at the middle

school, high school, undergraduate, and graduate levels the opportunity to participate in the exploration of Mars by planning, acquiring, and analyzing real images of Mars. The THEMIS Student Imaging Program provides background information and teacher mentoring on Mars science to enable classes to plan independent science projects at Mars using THEMIS observations.

Individual classes (grades 5–12) throughout the U.S. research Mars and prepare a short science rational for a target site in conjunction with mentoring and support by the THEMIS staff. The THEMIS staff reviews the student proposals and selects participants. It is expected that approximately 150 classes will participate each year, with high schools selected from each of the 50 states. When possible, selected members of these classes will travel to ASU during the week of image acquisition. The remainder of class will participate in the data acquisition via the Web and through emails, interactive interviews, journals, etc that are designed and implemented by the students. Following the image acquisition, each class will analyze their image in the context of the initial hypothesis- based question that they formulated.

Undergraduate and graduate students or classes participate at a higher level that involves a more detailed specification of a Mars research project. These students prepare a short science rational for a target site and a specific hypothesis to be tested. Students interact with the THEMIS staff to plan image acquisition, and travel to ASU during image acquisition as appropriate or participate via Web interaction. The students analyze their images and participate in a yearly workshop held at ASU. Where appropriate, these projects will be published in the scientific literature.

Acknowledgements

We wish to extend our sincere thanks to all those individuals who have contributed to the detailed design and implementation of this investigation. The highly dedicated team of engineers at Raytheon Santa Barbara Remote Sensing, led by Teresa Fortuna, Martin Greenfield, John Jeffryes, Robert Jensen, Bronislaus Kopra, Chris Laufer, Philip Mayner, Andy Mills, Bill O'Donnell, Paul Owens, Mike Pavlov, George Polchin, and Tom Sprafka, made major contributions to the hardware development. Paul Otjens and Jeff Lewis made major contributions to the VIS engineering at MSSS. Dick Chandos and Spencer Lee provided significant assistance in the final instrument testing and integration. Noel Gorelick, Ben Steinberg, Michael Weiss-Malik, and Saadat Anwar have participated in software development at Arizona State University. Teresa Robinette, Nancy Walizer, and Tara Fisher made major contributions to the administration of this investigation. Carl Kloss provided excellent management of this investigation at the Jet Propulsion Laboratory, and Tim Schofield provided the scientific interface with the Mars Global

Surveyor Project Office. Reviews by Jack Salisbury and two anonymous reviewers significantly improved the manuscript.

References

Bandfield, J. L., 2002, Global mineral distributions on Mars, *J. Geophys. Res.* **107**, 10.1029/2001JE001510.

Bandfield, J. L., Hamilton, V. E. and Christensen, P. R.: 2000a, A global view of Martian volcanic compositions, *Science* **287**, 1626–1630.

Bandfield, J. L., Smith, M. D. and Christensen, P.R.: 2000b, Spectral dataset factor analysis and endmember recovery: Application to analysis of martian atmospheric particulates, *J. Geophys. Res.* **105**, 9573–9588.

Bargar, K. E.: 1978, Geology and thermal history of Mammoth Hot Springs, Yellowstone National Park, Wyoming, *U.S. Geol. Surv. Bull.* **1444**, 55 pp.

Bartholomew, M. J., Kahle, A. B. and Hoover, G.: 1989, Infrared spectroscopy (2.3–20 μm) for the geological interpretation of remotely-sensed multispectral thermal infrared data, *Int. J. Remote Sensing* **10**, 529–544.

Bell, J. F., III, McCord, T. B. and Owensby, P. D.: 1990, Observational evidence of crystalline iron oxides on Mars, *J. Geophys. Res.* **95**, 14447–14461.

Bell, J. F., III, McSween, H. Y., Murchie, S. L., Johnson, J. R., Reid, R., Morris, R. V., Anderson, R. C., Bishop, J. .L., Bridges, N. T., Britt, D. T., Crisp, J. A., Economou, T., Ghosh, A., Greenwood, J. P., Gunnlaugsson, H. P., Hargraves, R. M., Hviid, S., Knudsen, J. M., Madsen, M. B., Moore, H. J., Reider, R., and Soderblom, L.: 2000, Mineralogic and compositional properties of Martian soil and dust: Results from Mars Pathfinder, *J. Geophys. Res.* **105**, 1721–1755.

Blaney, D. L. and McCord, T. B.: 1995, Indications of sulfate minerals in the martian soil from Earth-based spectroscopy, *J. Geophys. Res.* **100**, 14,433–14,441.

Boston, P. J., Ivanov, M. V. and McKay, C. P.: 1992, On the possibility of chemosynthetic ecosystems in subsurface habitats on Mars, *Icarus* **95**, 300–308.

Brock, T. D.: 1978, *Thermophilic Microorganisms and Life at High Temperatures*, Springer-Verlag, New York.

Burns, R. G.: 1993, Origin of electronic spectra of minerals in the visible to near-infrared region, in *Remote Geochemical Analysis: Elemental and Mineralogical Composition*, edited by C.M. Pieters, and P.A.J. Englert, Cambridge University Press.

Carr, M. H.: 1996, *Water on Mars*, Oxford Univ. Press, New York.

Christensen, P. R., Bandfield, J. L., Hamilton, V. E., Howard, D. A., Lane, M. D., Piatek, J. .L., Ruff, S. W., and Stefanov, W. L.: 2000a, 'A thermal emission spectral library of rock forming minerals', *J. Geophys. Res.* **105**, 9735–9738.

Christensen, P. R., Bandfield, J. L., Hamilton, V. E., Ruff, S. W., Kieffer, H. H, Titus, T., Malin, M. C., Morris, R. V., Lane, M. D., Clark, R. N., Jakosky, B. M., Mellon, M. T., Pearl, J. C., Conrath, B. J., Smith, M. D., Clancy, R. T., Kuzmin, R. O., Roush, T., Mehall, G. L., Gorelick, N., Bender, K., Murray, K., Dason, S., Greene, E., Silverman, S. H., and Greenfield, M.: 2001a, 'The Mars Global Surveyor Thermal Emission Spectrometer experiment: Investigation description and surface science results', *J. Geophys. Res.* **106**, 23,823–23,871.

Christensen, P. R., Bandfield, J. L., Smith, M. D., Hamilton, V. E., and Clark, R. N.: 2000b, 'Identification of a basaltic component on the Martian surface from Thermal Emission Spectrometer data', *J. Geophys. Res.* **105**, 9609–9622.

Christensen, P. R., Clark, R. N., Kieffer, H. H., Malin, M. C., Pearl, J. C., Bandfield, J. L., Edgett, K. S., Hamilton, V. E., Hoefen, T., Lane, M. D., Morris, R. V., Pearson, R., Roush, T., Ruff, S. W., and Smith, M. D.: 2000c, 'Detection of crystalline hematite mineralization on Mars by the

Thermal Emission Spectrometer: Evidence for near-surface water', *J. Geophys. Res.* **105**, 9623–9642.

Christensen, P. R. and Harrison, S. T.: 1993, 'Thermal infrared emission spectroscopy of natural surfaces: Application to desert varnish coatings on rocks', *J. Geophys. Res.* **98**(B11), 19,819–19,834.

Christensen, P. R., Malin, M. C., Morris, R. V., Bandfield, J., Lane, M. D., and Edgett, K.: 2000d, 'The distribution of crystalline hematite on Mars from the Thermal Emission Spectrometer: Evidence for liquid water', *Lunar and Planet. Sci.* **XXX**, Abstract # 1627.

Christensen, P. R., Malin, M. C., Morris, R. V., Bandfield, J. L., and Lane, M. D.: 2001b, 'Martian hematite mineral deposits: Remnants of water-driven processes on early Mars, *J. Geophys. Res.* **106**, 23,873–23,885.

Christensen, P. R. and Zurek, R. W.: '1984, Martian north polar hazes and surface ice: Results from the Viking survey/completion mission', *J. Geophys. Res.* **89**, 4587–4596.

Clark, R. N., Swayze, G. A., Singer, R. B., and Pollack, J. B.: 1990, 'High-resolution reflectance spectra of Mars in the 2.3 μm region: Evidence for the mineral scapolite', *J. Geophys. Res.* **95**, 14,463–14,480.

Conel, J. E.: 1969, 'Infrared emissivities of silicates: Experimental results and a cloudy atmosphere model of spectral emission from condensed particulate mediums', *J. Geophys. Res.* **74**, 1614–1634.

Conrath, B., Curran, R., Hanel, R., Kunde, V., Maguire, W., Pearl, J., Pirraglia, J., and Walker, J.: 1973, 'Atmospheric and surface properties of Mars obtained by infrared spectroscopy on Mariner 9', *J. Geophys. Res.* **78**, 4267–4278.

Conrath, B. J., Pearl, J. C., Smith, M. D., Maguire, W. C., Christensen, P. R., Dason, S., and Kaelberer, M.S.: 2000, 'Mars Global Surveyor Thermal Emission Spectrometer (TES) Observations: Atmospheric temperatures during aerobraking and science phasing', *J. Geophys. Res.* **105**, 9509–9520.

Craddock, R. A. and Maxwell, T. A.: 1993, 'Geomorphic evolution of the Martian highlands through ancient fluvial processes', *J. Geophys. Res.* **98**, 3453–3468.

Craddock, R. A., Maxwell, T. A., and Howard, A. D.: 1997, 'Crater morphometry and modification in the Sinus Sabaeus and Margaritifer Sinus regions of Mars', *J. Geophys. Res.* **102**, 13,321–13,340.

Crisp, J., Kahle, A. B., and Abbott, E. A.: 1990, 'Thermal infrared spectral character of Hawaiian basaltic glasses', *J. Geophys. Res.* **95**, 21657–21669.

Davies, D. W., Farmer, C. B., and LaPorte, D. D.: 1977, 'Behavior of volatiles in Mars' polar areas: A model incorporating new experimental data', *J. Geophys. Res.* **82**, 3815–3822.

Edgett, K. S.: 1995, 'To Mars by way of the schoolhouse', *Mercury* **24**, 28–31.

Edgett, K. S. and Christensen, P. R.: 1995, 'Multispectral thermal infrared observations of sediments in volcaniclastic aeolian dune fields: Implications for the Mars Global Surveyor Thermal Emission Spectrometer', *Lunar Planet. Sci.* **XXVI**, 355–356.

Edgett, K. S., Christensen, P. R., Dieck, P. A., Kingsbury, A. R., Kuhlman, S. D., Roberts, J. L., Wakefield, D. A., Rice, J. W. J., and Dodds, J.: 1997, 'K-12 and public outreach for NASA flight projects: Five years (1992–1997) of the Arizona Mars K-12 Education Program', *Lunar Planet. Sci.* **28**, 323–324.

Edgett, K. S. and Rice, J. W. J.: 1995, 'Summary of education and public outreach in Mars Pathfinder Landing Site Workshop II', *LPI Tech. Rept.* **95–01** (Part 2), 17–29.

Edgett, S. K. and Christensen, P. R.: 1996, 'K-12 education outreach program initiated by a university research team for the Mars Global Surveyor Thermal Emission Spectrometer project', *J. Geoscience Education* **44**, 183–188.

Ellis, A. J. and McMahon, W. A. J.: 1977, *Chemistry and Geothermal Systems*, Academic Press, New York.

Exobiology_Working_Group: 1995, An Exobiological Strategy for Mars Exploration, NASA Headquarters.

Farmer, V. C.: 1974, *The Infrared Spectra of Minerals*, 539 pp., Mineralogical Society, London.

Feely, K. C. and Christensen, P. R.: 1999, 'Quantitative compositional analysis using thermal emission spectroscopy: Application to igneous and metamorphic rocks', *J. Geophys. Res.* **104**, 24,195–24,210.

Gaffey, S. J.: 1984, Spectral reflectance of carbonate minerals and rocks in the visible and infrared (0.35 to 2.55 μm) and its applications in carbonate petrology, Ph.D. thesis, University of Hawaii.

Gillespie, A. R., Kahle, A. B., and Palluconi, F. D.: 1984, 'Mapping alluvial fans in Death Valley, CA, using multichannel thermal infrared images', *Geophys. Res. Ltr.* **11**(11), 1153–1156.

Golombek, M. P., Cook, R. A., Moore, H. J., and Parker, T. J.: 1997, 'Selection of the Mars Pathfinder landing site', *J. Geophys. Res.* **102**, 3967–3988.

Greeley, R., Lancaster, N., Lee, S., and Thomas, P.: 1992, Martian Eolian Processes, Sediments, and Features, in *Mars*, edited by H. Kieffer, B. Jakosky, C. Snyder, and M. Matthews, Univ. of Arizona Press, Tucson.

Haberle, R. M. and Jakosky, B. M.: 1990, 'Sublimation and transport of water from the north residual polar cap on Mars', *J. Geophys. Res.* **95**(B2), 1423–1437.

Hamilton, V. E.: 1999, 'Linear deconvolution of mafic igneous rock spectra and implications for interpretation of TES data', *Lunar and Planet. Sci.* **XXX**, CD-ROM, Abstract 1825.

Hamilton, V. E.: 2000, 'Thermal infrared emission spectroscopy of the pyroxene mineral series', *J. Geophys. Res.* **105**, 9701–9716.

Hamilton, V. E. and Christensen, P. R.: 2000, 'Determination of modal mineralogy of mafic and ultramafic igneous rocks using thermal emission spectroscopy', *J. Geophys. Res.* **105**, 9717–9734.

Hamilton, V. E., Wyatt, M. B., McSween, H. Y., and Christensen, P. R.: 2001, 'Analysis of terrestrial and martian volcanic compositions using thermal emission spectroscopy: II. Application to martian surface spectra from MGS TES', *J. Geophys. Res.* **106**, 14,733–14,747.

Hanel, R. A., Conrath, B. J., Hovis, W. A., Kunde, V. G., Lowman, P. D., Pearl, J. C., Prabhakara, C., Schlachman, B., and Levin, G. V.: 1972, 'Infrared spectroscopy experiment on the Mariner 9 mission: Preliminary results', *Science* **175**, 305–308.

Hapke, B.: 1981, 'Bidirectional reflectance spectroscopy I. Theory', *J. Geophys. Res.* **86**, 3039–3054.

Hapke, B.: 1993, Combined Theory of Reflectance and Emittance Spectroscopy, in *Remote Geochemical Analysis: Elemental and Mineralogical Composition*, edited by C. M. Pieters and P. A. J. Englert, Cambridge University Press, Cambridge.

Henderson, B. G., Jakosky, B., and Randall, C. E.: 1992, 'A Monte Carlo Model of Polarized Thermal Emission from Particulate Planetary Surfaces', *Icarus* **99**, 51–62.

Herkenhoff, K. E., and Murray, B. C.: 1990a, 'Color and albedo of the south polar layered deposits on Mars', *J. Geophys. Res.* **95**, 14,511–14,529.

Herkenhoff, K. E. and Murray, B. C.: 1990b, 'High-resolution topography and albedo of the south polar layered deposits on Mars', *J. Geophys. Res.* **95**, 14,511–14,529.

Hook, S. J., Karlstrom, K. E., Miller, C. F., and McCaffrey, K. J. W.: 1994, 'Mapping the Piute Mountains, California, with thermal infrared multispectral scanner (TIMS) images', *J. Geophys. Res.* **99**, 15,605–15,622.

Hunt, G. R. and Logan, L. M.: 1972, 'Variation of single particle mid-infrared emission spectrum with particle size', *Appl. Opt.* **11**, 142–147.

Hunt, G. R. and Salisbury, J. W.: 1970, 'Visible and near-infrared spectra of minerals and rocks: I. Silicate minerals', *Mod. Geol.* **1**, 283–300.

Hunt, G. R., and Salisbury, J. W.: 1976, 'Mid-infrared spectral behavior of metamorphic rocks', *Environ. Res. Paper*, 543-AFCRL-TR-76-0003, 67.

Hunt, G. R. and Vincent, R. K.: 1968, 'The behavior of spectral features in the infrared emission from particulate surfaces of various grain sizes', *J. Geophys. Res.* **73**, 6039–6046.

Jakosky, B. M.: 1998, *The Search for Life on Other Planets*, 336 pp., Cambridge Univ. Press.

Jakosky, B. M., Mellon, M. T., Kieffer, H. H., Christensen, P. R., Varnes, E. S., and Lee, S. W.: 2000, 'The thermal inertia of Mars from the Mars Global Surveyor Thermal Emission Spectrometer', *J. Geophys. Res.* **105**, 9643–9652.

Jakosky, B. M. and Shock, E. L.: 1998, 'The biological potential of Mars, the early Earth, and Europa', *J. Geophys. Res.* **103**, 19359–19364.

James, P. B. and North, G. R.: 1982, 'The seasonal CO2 cycle on Mars: An application of an energy balance climate model', *J. Geophys. Res.* **87**, 10,271–10,284.

Johnson, J. R., Christensen, P. R., and Lucey, P. G.: in press, 'Dust coatings on basalt and implications for thermal infrared spectroscopy of Mars', *J. Geophys. Res.*

Kahle, A., Palluconi, F. D., and Christensen, P. R.: 1993, Thermal emission spectroscopy: Application to Earth and Mars, in *Remote Geochemical Analysis: Elemental and Mineralogical Composition*, edited by C.M. Pieters, and P.A.J. Englert, pp. 99–120, Cambridge University Press, Cambridge.

Kahle, A. B., Madura, D. P., and Soha, J. M.: 1980, 'Middle infrared multispectral aircraft scanner data: Analysis for geological applications', *Appl. Optics* **19**, 2279–2290.

Kieffer, H. H.: 1979, 'Mars south polar spring and summer temperatures: A residual CO2 frost', *J. Geophys. Res.* **84**, 8263–8289.

Kieffer, H. H.: 1990, 'H2O grain size and the amount of dust in Mars' residual north polar cap', *J. Geophys. Res.* **95**, 1481–1494.

Kieffer, H. H., Martin, T. Z., Peterfreund, A. R., Jakosky, B. M., Miner, E. D., and Palluconi, F. D.: 1977, 'Thermal and albedo mapping of Mars during the Viking primary mission', *J. Geophys. Res.* **82**, 4249–4292.

Kieffer, H. H., Titus, T., Mullins, K., and Christensen, P. R.: 2000, 'Mars south polar cap as observed by the Mars Global Surveyor Thermal Emission Spectrometer', *J. Geophys. Res.* **105**, 9653–9700.

Kieffer, H. H. and Zent, A. P.: 1992, 'Quasi-periodic climatic change on Mars, in *Mars*, edited by H. H. Kieffer, B. M. Jakosky, C. W. Snyder, and M. S. Matthews, Univ. of Arizona Press, Tucson.

Komatsu, G. and Baker, V. R.: 1997, 'Paleohydrology and flood geomorphology of Ares Vallis', *J. Geophys. Res.* **102**, 4151–4160.

Lane, M. D. and Christensen, P. R.: 1997, 'Thermal infrared emission spectroscopy of anhydrous carbonates', *J. Geophys. Res.* **102**, 25,581–25,592.

Lazerev, A. N.: 1972, *Vibrational spectra and structure of silicates*, 302 pp., Consultants Bureau, New York.

Lyon, R. J. P.: 1962, Evaluation of infrared spectroscopy for compositional analysis of lunar and planetary soils, in *Stanford Research Institute Final Report Contract NASr*, Stanford Research Institute.

Malin, M. C. and Carr, M. H.: 1999, 'Groundwater formation of martian valleys', *Nature* **397**, 589–591.

Malin, M. C. and Edgett, K. S.: 2000, 'Sedimentary rocks of early Mars', *Science* **290**, 1927–1937.

Malin, M. C. and Edgett, K. S.: 2001, 'Mars Global Surveyor Mars Orbiter Camera: Interplanetary cruise through primary mission', *J. Geophys. Res.* **106**, 23,429–23,570.

Martin, T. Z.: 1986, 'Thermal infrared opacity of the mars atmosphere', *Icarus* **66**, 2–21.

McCord, T. B., Clark, R. N., and Singer, R. B.: 1982, 'Mars: Near-infrared reflectance spectra of surface regions and compositional implications', *J. Geophys. Res.* **87**, 3021–3032.

McKay, D. S., E. K. G. Jr., Thomas-Keprta, K. L., Vali, H., Romanek, C. S., Clemett, S. J., Chillier, X. D. F., Maechling, C. R., and Zare, R. N.: 1996, 'Search for past life on Mars: Possible relic biogenic activity in martian meteorite ALH84001', *Science* **273**, 924–930.

McSween, H. Y., Jr.: 1994, 'What have we learned about Mars from SNC meteorites', *Meteoritics* **29**, 757–779.

Mellon, M. T., Jakosky, B. M., Kieffer, H. H., and Christensen, P. R.: 2000, 'High resolution thermal inertia mapping from the Mars Global Surveyor Thermal Emission Spectrometer', *Icarus* **148**, 437–455.

Moersch, J. E. and Christensen, P. R.: 1995, 'Thermal emission from particulate surfaces: A comparison of scattering models with measured spectra', *J. Geophys. Res.* **100**, 7,465–7,477.

Morris, R. V., Gooding, J. L., Lauer, J. H. V., and Singer, R. B.: 1990, 'Origins of Marslike spectral and magnetic properties of a Hawaiian palagonitic soil', *J. Geophys. Res.* **95**, 14,427–14,435.

Mustard, J. F., Erard, S., Bibring, J.-P., Head, J. W., Hurtrez, S., Langevin, Y., Pieters, C. M., and Sotin, C. J.: 1993, 'The surface of Syrtis Major: Composition of the volcanic substrate and mixing with altered dust and soil', *J. Geophys. Res.* **98**, 3387–3400.

Mustard, J. F. and Hays, J. E.: 1997, 'Effects of hyperfine particles on reflectance spectra from 0.3 to 25 μm', *Icarus* (125), 145–163.

Mustard, J. F. and Sunshine, J. M.: 1995, 'Seeing through the dust: Martian crustal heterogeneity and links to the SNC meteorites', *Science* **267**, 1623–1626.

Nash, D. B. and Salisbury, J. W.: 1991, 'Infrared reflectance spectra of plagioclase feldspars', *Geophys. Res. Lett.* **18**, 1151–1154.

Paige, D. A. and Ingersoll, A. P.: 1985, 'Annual heat balance of martian polar caps: Viking observations', *Science* **228**, 1160–1168.

Palluconi, F. D. and Meeks, G. R.: 1985, Thermal infrared multispectral scanner (TIMS): An investigator's guide to TIMS data, Jet Propulsion Laboratory.

Pearl, J. C., Smith, M. D., Conrath, B. J., Bandfield, J. L., and Christensen, P. R.: 2001, 'Observations of water-ice clouds by the Mars Global Surveyor Thermal Emission Spectrometer experiment: The first martian year', *J. Geophys. Res.* 12,325–12,338.

Pentecost, A.: 1996, High Temperature Ecosystems and their Chemical Interactions with their Environment, in *Evolution of Hydrothermal Ecosystems on Earth (and Mars?)*, edited by G. R. Bock, and J. A. Goode, pp. 99–111, John Wiley and Sons, Chichester.

Pimentel, G. C., Forney, P. B., and Herr, K. C.: 1974, 'Evidence about hydrate and solid water in the martian surface from the 1969 Mariner infrared spectrometer', *J. Geophys. Res.* **79** (No. 11), 1623–1634.

Ramsey, M. S.: 1996, Quantitative Analysis of Geologic Surfaces: A Deconvolution Algorithm for Midinfrared Remote Sensing Data, Ph.D Dissertation thesis, Arizona State University.

Ramsey, M. S. and Christensen, P. R.: 1992, The linear 'un-mixing' of laboratory thermal infrared spectra: Implications for the Thermal Emission Spectrometer (TES) experiment, Mars Observer, *Lunar & Planet. Sci.* **XXIII**, 1127–1128.

Ramsey, M. S. and Christensen, P. R.: 1998, 'Mineral abundance determination: Quantitative deconvolution of thermal emission spectra', *J. Geophys. Res.* **103**, 577–596.

Ramsey, M. S., Christensen, P. R., Lancaster, N., and Howard, D .A.: 1999, 'Identification of sand sources and transport pathways at Kelso Dunes, California using thermal infrared remote sensing', *Geol. Soc. Am. Bull.* **111**, 636–662.

Roush, T. L., Blaney, D. L., and Singer, R. B.: 1993, The surface composition of Mars as inferred from spectroscopic observations, in *Remote Geochemical Analysis: Elemental and Mineralogical Composition*, edited by C. M. Pieters, and P. A. J. Englert, Cambridge University Press.

Ruff, S. W. and Christensen, P. R.: 2002, 'Bright and dark regions on Mars: Particle size and mineralogical characteristics based on Thermal Emission Spectrometer data', *J. Geophys. Res.*, in press.

Salisbury, J. W.: 1993, Mid-infrared spectroscopy: Laboratory data, in *Remote Geochemical Analysis: Elemental and Mineralogical Composition*, edited by C. Pieters, and P. Englert, pp. Ch. 4, Cambridge University Press, Cambridge.

Salisbury, J. W., D'Aria, D. M., and Jarosewich, E.: 1991, 'Mid-infrared (2.5–13.5 um) reflectance spectra of powdered stony meteorites', *Icarus* **92**, 280–297.

Salisbury, J. W. and Eastes, J. W.: 1985, 'The effect of particle size and porosity on spectral contrast in the mid-infrared', *Icarus* **64**, 586–588.

Salisbury, J. W., Hapke, B., and Eastes, J. W.: 1987a, 'Usefulness of weak bands in midinfrared remote sensing of particulate planetary surfaces', *J. Geophys. Res.* **92**, 702–710.

Salisbury, J. W. and Wald, A.: 1992, 'The role of volume scattering in reducing spectral contrast of reststrahlen bands in spectra of powdered minerals', *Icarus* **96**, 121–128.

Salisbury, J. W., Wald, A., and D'Aria, D. M.: 1994, 'Thermal-infrared remote sensing and Kirchhoff's law 1. Laboratory measurements', *J. Geophys. Res.* **99**, 11897–11911.

Salisbury, J. W. and Walter, L. S.: 1989, 'Thermal infrared (2.5–13.5 μm) spectroscopic remote sensing of igneous rock types on particulate planetary surfaces', *J. Geophys. Res.* **94**(No. B7), 9192–9202.

Salisbury, J. W., Walter, L. S., and Vergo, N.: 1987b, Mid-infrared (2.1–25 μm) spectra of minerals: First Edition, in *U.S.G.S., Open File Report*, pp. 87–263, U. S. Geological Survey Open File Report.

Selivanov, A. S., Naraeva, M. K., Panfilov, A. S., Gektin, Y. M., Kharlamov, V. D., Romanov, A. V., Fomin, D. A., and Miroshnichenko, Y. Y.: 1989, 'Thermal imaging of the surface of Mars', *Nature* **341**, 593–595.

Shock, E. L.: 1997, 'High temperature life without photosynthesis as a model for Mars', *J. Geophys. Res.*

Shoemaker, E. M.: 1963, Impact mechanics at Meteor Crater, Arizona, in *The Moon, Meteorites, and Comets*, edited by B. M. Middlehurst, and G. P. Kuiper, pp. 301–336, Univ. of Chicago Press, Chicago.

Silverman, S., Bates, D., Schueler, C., O'Donnell, B., Christensen, P., Mehall, G., Tourville, T. and Cannon, G.: 1999, Miniature Thermal Emission Spectrometer for the Mars 2001 Lander, *Proceedings of the IEEE*.

Singer, R. B.: 1982, 'Spectral evidence for the mineralogy of high-albedo soils and dust on Mars', *J. Geophys. Res.* **87**, 10,159–10,168.

Smith, M. D., Bandfield, J. L., and Christensen, P. R.: 2000, 'Separation of atmospheric and surface spectral features in Mars Global Surveyor Thermal Emission Spectrometer (TES) spectra: Models and atmospheric properties', *J. Geophys. Res.* **105**, 9589–9608.

Smith, M. D., Conrath, B. J., Pearl, J. C., and Christensen, P. R.: 2002, 'Thermal Emission Spectrometer observations of martian planet-encircling dust storm 2001A', *Icarus* **157**, 259–263.

Smith, M. D., Pearl, J. C., Conrath, B. J., and Christensen, P. R.: 2001a, 'Thermal Emission Spectrometer results: Mars atmospheric thermal structure and aerosol distribution', *J. Geophys. Res.* **106**, 23929–23945.

Smith, M. D., Pearl, J. C., Conrath, B. J., and Christensen, P. R.: 2001b, 'One Martian year of atmospheric observations by the Thermal Emission Spectrometer', *Geophys. Res. Letters* **28**, 4263–4266.

Smith, M. D., Pearl, J. C., Conrath, B. J., and Christensen, P. R.: 2001c, 'Thermal Emission Spectrometer results: Atmospheric thermal structure and aerosol distribution', *J. Geophys. Res.* **106**, 23,929–23,945.

Stevens, T. O. and McKinley, J. P.: 1995, 'Lithoautotrophic microbial ecosystems in deep basalt aquifers', *Science* **270**, 450–454.

Tamppari, L. K., Zurek, R. W., and Paige, D. A.: 2000, 'Viking era water ice clouds', *J. Geophys. Res.* **105**, 4087–4107.

Tanaka, K. L.: 1997, 'Sedimentary history and mass flow structures of Chryse and Acidalia Planitiae', *Mars, J. Geophys. Res.* **102**, 4131–4149.

Tanaka, K. L. and Leonard, G. J.: 1995, 'Geology and landscape evolution of the Hellas region of Mars', *J. Geophys. Res.* **100**, 5407–5432.

Thomas, P. and Gierasch, P. J.: 1995, 'Polar margin dunes and winds on Mars', *J. Geophys. Res.* **100**, 5379–5406.

Thomas, P. C., Malin, M. C., and Edgett, K. S.: 2000, 'North-south geological differences between the residual polar caps on Mars', *Nature* **404**, 161–164.

Thomas, P. C., Squyres, S., Herkenhoff, K., Howard, A., and Murray, B.: 1992, Polar deposits of Mars in Mars, in *Mars*, edited by H. Kieffer, B. Jakosky, C. Snyder, and M. Matthews, pp. 767–795, Univ. Arizona Press, Tucson.

Thomas, P. C. and Weitz, C.: 1989, 'Sand dune materials and polar layered deposits on Mars', *Icarus* **81**, 185–215.

Thomson, J. L. and Salisbury, J. W.: 1993, 'The mid-infrared reflectance of mineral mixtures (7–14 μm)', *Remote Sensing of Environment* **45**, 1–13.

Titus, T. N., Kieffer, H. H., Mullins, K. F., and Christensen, P. R.: 2001, 'TES Pre-mapping data: Slab ice and snow flurries in the Martian north polar night', *J. Geophys. Res.* **106**, 23,181–23,196.

Van der Marel, H. W. and Beeutelspacher, H.: 1976, Atlas of infrared spectroscopy of clay minerals and their admixtures, 396pp., Elsevier Scientific Publishing Co., Amsterdam.

Vincent, R. K. and Hunt, G. R.: 1968, 'Infrared reflectance from mat surfaces', *Appl. Opt.* **7**, 53–59.

Vincent, R. K. and Thompson, F.: 1972, 'Spectral compositional imaging of silicate rocks', *J. Geophys. Res.* **17** (No. 14), 2465–2472.

Wald, A. E. and Salisbury, J. W.: 1995, 'Thermal infrared emissivity of powdered quartz', *J. Geophys. Res.* **100**, 24665–24675.

Walter, M. R. and Des Marais, D. J.: 1993, 'Preservation of biological information in thermal spring deposits: Developing a strategy for the search for fossil life on Mars', *Icarus* **101**, 129–143.

White, D. E., Hutchinson, R. A., and Keith, T. E. C.: 1988, *The Geology and Remarkable Thermal Acitivty of Norris Geyser Basin, Yellowstone National Park*, U.S. Geol. Survey Prof. Paper 1456.

Wilson, E. B., Jr., Decius, J. C., and Cross, P. C.: 1955, *Molecular Vibrations: The Theory of Infrared and Raman Vibrational Spectra*, McGraw-Hill.

Wyatt, M. B.,, Hamilton, V. E., McSween, J. H. Y., Christensen, P. R., and Taylor, L. A.: 2001, 'Analysis of terrestrial and martian volcanic compositions using thermal emission spectroscopy: I. Determination of mineralogy, chemistry, and classification strategies', *J. Geophys. Res.* **106**, 14,711–14,732.

Young, J.: 1999a, FM1 Absolute radiometric calibration reflectance region: uncertainty estimate, Raytheon Santa Barbara Remote Sensing, Santa Barbara.

Young, J.: 1999b, FM1 Absolute radiometric calibration thermal region: uncertainty estimate, Raytheon Santa Barbara Remote Sensing, Santa Barbara.

Young, J.: 1999c, Summary of the Blackbody Calibration Source (BCS) and Space View Source (SVS) refurbishment and calibration process, Raytheon Santa Barbara Remote Sensing, Santa Barbara.